

Navier-Stokes bounds and scaling for compact trefoils in large $(2\ell\pi)^3$ domains.

Robert M. Kerr †,

Department of Mathematics, University of Warwick, Coventry CV4 7AL, United Kingdom

(Received 26 February 2025)

For a perturbed trefoil vortex knot evolving under the Navier-Stokes equations, a sequence of ν -independent times t_m are identified corresponding to a set of scaled, volume-integrated vorticity moments $\nu^{1/4}\mathcal{O}_{V_1}$ with this hierarchy $t_\infty \leq \dots \leq t_m \dots t_1 = t_x \approx 40$ and $\mathcal{O}_{V_m} = (\int_{V_\ell} |\omega|^{2m} dV)^{1/2m}$. For $Z(t) = \mathcal{O}_{V_1}(t)^2$ the volume-integrated enstrophy, convergence of $\sqrt{\nu}Z(t)$ at $t_x = t_1$ marks the end of the reconnection scaling phase. Physically, reconnection follows from the formation of a double vortex sheet, then a knot, which splits into spirals. Z then accelerates, leading to approximate finite-time ν -independent convergence of the energy dissipation rate $\epsilon(t) = \nu Z(t)$ at $t_\epsilon \sim 2t_x$ and sustained over a finite span $\Delta T_\epsilon \searrow 0.5t_\epsilon$, giving Reynolds number independent finite-time, dissipation, $\Delta E_\epsilon = \int_{\Delta T_\epsilon} \epsilon dt$, and thus satisfying one definition for a *dissipation anomaly*. Evidence for transient Kolmogorov-like enstrophy spectra is found over ΔT_ϵ . A critical factor in achieving these temporal convergence laws is how the domain $V_\ell = (2\ell\pi)^3$ is increased as $\ell \sim \nu^{-1/4}$, for $\ell = 2$ to 6, then to $\ell = 12$, as ν decreases. $(2\ell\pi)^3$ domain compatibility with established $(2\pi)^3$ mathematics in appendix allows small ν Navier-Stokes solutions. Two spans of ν are considered. Over the first factor of 25 decrease in ν , all of the $\nu^{1/4}\mathcal{O}_{V_m}(t)$ converge to their respective t_m . For the next factor of 5 decrease in ν , ℓ is increased to $\ell = 12$, there is only convergence of $\nu^{1/4}\mathcal{O}_{V_\infty}(t)$ to t_∞ and later $\sqrt{\nu}Z(t)$ convergence at $t_1 = t_x$ and $\epsilon(t)$ over $t \sim t_\epsilon$.

1. Background

Finite-energy dissipation is ubiquitous in turbulent, large Reynolds number, geophysical and engineering flows. Meaning that in these systems, observations show that their turbulent flows always develop Reynolds number, or viscosity ν , independent dissipation (Sreenivasan 1984; Vassilicos 2015). Forced simulations can generate finite-dissipation, but it is unclear what the pre-cursors to finite-dissipation might be if the flow is unforced. Can trefoil reconnection calculations (Kerr 2018b, 2023) fill that gap?

To fill that gap, this paper introduces this pre-cursor for trefoil knot analysis: Temporal convergence of $\nu^{1/4}$ scaled, volume-integrated vorticity moments, $\nu^{1/4}\mathcal{O}_{V_m}(t)$, with

$$\mathcal{O}_{V_m}(t) = \left(\int_{V_\ell} |\omega|^{2m} dV \right)^{1/2m} \quad \text{and} \quad \mathcal{O}_{V_1} \leq \dots \leq d_m \mathcal{O}_{V_m}(t) \leq \dots \leq d_\infty \mathcal{O}_\infty(t). \quad (1.1)$$

The hierarchy of convergence times is $t_\infty \leq \dots \leq t_m \dots t_1 = t_x$ and precedes the post-reconnection $t > t_x$ accelerated growth of the volume-integrated enstrophy $Z(t) = \mathcal{O}_{V_1}^2(t)$ (1.12) that leads to finite dissipation, with evidence from figure 4 for a numerical *dissipation anomaly*.

The definition of a numerical *dissipation anomaly* in this paper is convergence of this time-integral of the energy dissipation rate $\epsilon(t) = \nu Z(t)$ (Kerr 2023).

$$\Delta E_\epsilon = \int_0^{\Delta T_\epsilon} \epsilon dt > 0, \quad \text{with } \Delta T_\epsilon \text{ a finite time} . \quad (1.2)$$

† Email address for correspondence: Robert.Kerr@warwick.ac.uk

Note that $Z(t) = V_\ell \Omega_1^2(t) = \mathcal{O}_{V_1}^2$ (1.12), where Ω_1 is the standard first Sobolev vorticity moment (1.8). Unforced trefoil knot calculations (Kerr 2018b, 2023), both of which used algebraic initial vorticity profiles, have already found convergent ΔE_ϵ over modest (factor of 4-8) ratios of ν , but without corroborating analysis for turbulent scaling such as wavenumber spectra.

In answering the finite ΔE_ϵ (1.2) question, these secondary issues are also addressed.

- What makes these calculations different than the majority of existing vortex reconnection calculations (Yao & Hussain 2022)?

- To achieve finite ΔE_ϵ as ν decreases, the domain size $(2\ell\pi)^3$ must be increased. What is the dependence of ℓ upon ν and is this compatible with existing mathematics? The appendices describe the new mathematics.

- If finite ΔE_ϵ is achieved, is there evidence for any Kolmogorov scaling that underlies that? This will be shown using the temporal evolution of the enstrophy spectra.

The calculations used to determine ΔE_ϵ incorporate two elements from two recent sets of unforced trefoil knot calculations (Kerr 2018b, 2023), both of which used algebraic initial vorticity profiles and had modest ΔE_ϵ , but without corroborating analysis for turbulent scaling such as as wavenumber spectra.

The first element from Kerr (2018b) is that in order to achieve greater enstrophy growth and numerical convergent dissipation rates, the domain size \mathcal{L} must increase as the viscosity ν decreases (2.1), thus breaking the constraint imposed by using only $(2\pi)^3$ domains. And now justified mathematically in the appendices.

The second element is that Kerr (2023) shows why, due to their improved stability properties, algebraic vorticity profiles rather than the traditional Gaussian vorticity profiles (Yao & Hussain 2022) should be used

This paper combines those two elements to show how a range of small ν , moderately high Reynolds number Navier-Stokes simulations in large domains can, without forcing or parameterisations, get approximate temporal convergence of the dissipation rates $\epsilon(t) = \nu Z(t)$ at $t_\epsilon \approx 2t_x$ and consistent finite-time ΔE_ϵ . (1.2) at $t \sim 1.5t_\epsilon$. Along with addressing the additional secondary questions listed above.

For comparing results from several computational domains, trefoil vortex knots with algebraic vorticity profiles are an ideal initial condition because they are compact, do not have inherent boundary instabilities and interesting because the usual assumptions of isotropy are broken by the helical initial condition. Compact means that the trefoils can be isolated from the boundaries as both the energy and enstrophy die off rapidly as $r \rightarrow \infty$ and can be redone in multiple domains. To demonstrate that this initial condition is compact, figure 1 shows the $r_1 = 0.25$ perturbed trefoil initial condition (1.20), with several paths are taken from the centre of the trefoil, though its initial trajectory, and further out.

Details of the stability properties of the algebraic profile on the trefoil using the original formulation of Howard & Gupta (1962) have been given previously (Kerr 2023) Essentially what that formulation tells us is that a profile can be unstable if the Rayleigh inflection point criteria is violated. That instability does not develop when algebraic profiles are used (Kerr 2023), but can form for Gaussian/Lamb-Oseen profiles. However, ‘can form’ does not necessarily mean ‘must form’, and what determines that difference mathematically is whether the initial perturbations break through ill-defined critical layers (Gallay & Smets 2020). Kerr (2023) shows that when mapping a strongly curved vortex trajectory onto a Cartesian mesh, the resulting field is not perfectly solenoidal and that after the necessary solenoidal correction is imposed, a large seed is created, one large enough to allow the Gaussian profile instability to grow. This observation probably applies to most of the calculations discussed in a recent review (Yao & Hussain 2022).

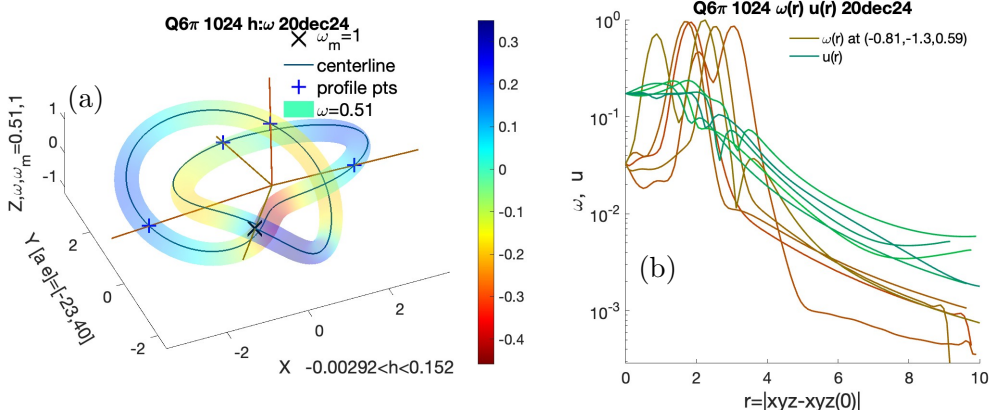


FIGURE 1. Perturbed trefoil initial condition. (a) $\omega = 0.51$ isosurface with $\omega_m = 1$, centreline vortex seeded at $\omega_m = 1$ plus centreline point through which several paths are taken. (b) Profiles of $\omega_j(r)$ taken through those points. For all the paths $\mathbf{s}_j(r)$, $\omega_j(r) \rightarrow 0$ exponentially as r grows. Confirming that the initial condition is compact.

However, this seed does not form if the initial vortices in a three-dimensional fluid are straight as in Zuccoli *et al.* (2024) and Ostillo-Monico *et al.* (2021). So there are still many situations when use of a Gaussian profile is legitimate.

Is there an early time diagnostic, supported by mathematics, that shows whether increasing the domain is a viable approach? Fortunately by using the volume-integrated enstrophy Z (1.12) as the diagnostic, instead of the volume-averaged enstrophy $Z_\Omega = \Omega_\Omega^2$ (1.8), temporal convergence can be achieved using $\sqrt{\nu}Z(t)$ at intermediate fixed times $t = t_x$. With section 1.3 and the appendices showing that this empirical large-domain observation is compatible with, through rescaling, a previously strictly $(2\pi)^3$ analytic result (Constantin 1986).

Where have observations identified convergent energy dissipation? Historically, one means is to use controlled experiments of turbulent flows to determine a dissipation coefficient C_ϵ , gotten by comparing the measured dissipation rate ϵ to the large scale dimensional estimate as follows:

$$\epsilon = C_\epsilon \mathcal{U}^3 / \mathcal{L} \sim C_\epsilon r_f^2 / t_{NL}^3, \quad (1.3)$$

where \mathcal{U} and \mathcal{L} are the large-scale velocity and length (Vassilicos 2015). For the trefoil one can use its diameter $\mathcal{L} = 2r_f$ (1.20) and for a ‘turbulent’ velocity \mathcal{U} , one can chose $\mathcal{U} = \|u\|_\infty(t_\epsilon)$, the maximum velocity at t_ϵ , the time with the largest dissipation rate ϵ (1.11) from figure 4. This is also when spectra show signs of Kolmogorov scaling in subsection 3.1. Early grid turbulence and jet data showed that C_ϵ is independent of the Reynolds number (Sreenivasan 1984), a conclusion that could even be applied to nonequilibrium turbulence as here (Vassilicos 2015). However, recent results (Schmitt *et al.* 2024) suggest that the large-scale coefficient C_ϵ depends on the properties of the small scale intermittency. Those are the experimental results that are used for the comparisons in the inset of figure 4.

The paper is organised as follows. First the equations are introduced, followed by a discussion of why simulations in large domains were required, including a summary of the new mathematics qualitatively supporting the previous empirical conclusions. This is followed by the extended numerical results for both $1/(\sqrt{\nu}Z(t))^{1/2}$ and $\epsilon(t) = \nu Z$ scaling, including evidence for a *dissipation anomaly* and additional examples of $t \lesssim t_x$, $\nu^{1/4}O_{Vm}(t)$ convergence. Resolution requirements are mentioned in section 1.4 and

discussed further in section 2.2. Section 3 provides the evidence for turbulent-like spectra and finally in section 4, some $t \lesssim t_x$ three-dimensional vortical structures are shown. Structures that are examples of how the $t > t_x$ range with finite dissipation forms. The appendix extends $(2\ell\pi)^3$, $\ell = 1$ Sobolev H^s analysis to larger $\ell > 1$, $(2\ell\pi)^3$ domains, showing that as ℓ grows there is relaxation of the analytic/Sobolev critical viscosities ν_s that enforce bounds upon the evolution of still smaller viscosities. These ν_s decrease as ℓ increases, which in turn allows convergence of the dissipation rates $\epsilon = \nu Z$ as ν decreases.

1.1. Governing equations

This paper primarily uses the incompressible $\nu \sim Re^{-1} \neq 0$ viscous Navier-Stokes velocity equations

$$\frac{\partial \mathbf{v}}{\partial t} + (\mathbf{v} \cdot \nabla) \mathbf{v} = -\nabla p + \underbrace{\nu \Delta \mathbf{v}}_{\text{viscous drag}}, \quad \nabla \cdot \mathbf{v} = 0, \quad (1.4)$$

and for additional analysis, the inviscid $\nu \equiv 0$ Euler equations

$$\frac{\partial \mathbf{u}}{\partial t} + (\mathbf{u} \cdot \nabla) \mathbf{u} = -\nabla p. \quad (1.5)$$

This includes the equation for their difference $\mathbf{w} = \mathbf{v} - \mathbf{u}$, which by replacing \mathbf{v} by $\mathbf{w} + \mathbf{u}$ throughout becomes

$$\mathbf{w}_t + \nu \Delta \mathbf{w} = -\nu \Delta \mathbf{u} - \underbrace{(\mathbf{w} \cdot \nabla) \mathbf{w}}_{B_{NL}(\mathbf{w}, \mathbf{w})} - \underbrace{(\mathbf{u} \cdot \nabla) \mathbf{w}}_{B_{NL}(\mathbf{u}, \mathbf{w})} - \underbrace{(\mathbf{w} \cdot \nabla) \mathbf{u}}_{B_{NL}(\mathbf{w}, \mathbf{u})} - \nabla p_w - \nabla p_u. \quad (1.6)$$

The Constantin & Foias (1988) notation $B_{NL}(\mathbf{u}, \mathbf{v}) = (\mathbf{u} \cdot \nabla) \mathbf{v}$ has been added to emphasize the similarities between how the three nonlinear terms are treated in section A.3.

The equation for the vorticity $\boldsymbol{\omega} = \nabla \times \mathbf{v}$ is

$$\frac{\partial \boldsymbol{\omega}}{\partial t} + (\mathbf{v} \cdot \nabla) \boldsymbol{\omega} = (\boldsymbol{\omega} \cdot \nabla) \mathbf{v} + \nu \Delta \boldsymbol{\omega}, \quad \nabla \cdot \boldsymbol{\omega} = 0. \quad (1.7)$$

and in fixed domains V_ℓ the vorticity moments obey this hierarchy

$$\Omega_m(t) = \left(V_\ell^{-1} \int_{V_\ell} |\boldsymbol{\omega}|^{2m} dV \right)^{1/2m} \quad (1.8)$$

with $\Omega_1(t) \leq c_2 \Omega_2(t) \leq \dots \leq c_m \Omega_m(t) \leq \dots \leq c_\infty \Omega_\infty(t)$. This ordering represents a type of Hölder inequality where the c_m are V_ℓ -dependent constants. These moments, scaled by characteristic frequencies, have been used in several recent papers (Kerr 2013a,b; Donzis *et al.* 2013).

However, the moments to be used in this paper are based on volume integration, $\mathcal{O}_{V_m}(t)$ (1.1) with an equivalent hierarchy $\mathcal{O}_{V_1} \leq \dots \leq d_m \mathcal{O}_{V_m}(t) \leq \dots \leq d_\infty \mathcal{O}_\infty(t)$. Note that $\Omega_\infty = \|\boldsymbol{\omega}\|_\infty$ is at the high end of both hierarchies, and at the other end, the volume-integrated enstrophy can be written as $Z(t) = V_\ell \Omega_1^2(t) = \mathcal{O}_{V_1}^2$.

For a compact vortex knot, the circulations Γ_i about its vortex structures are:

$$\Gamma_i = \oint_{\mathcal{C}_i} \mathbf{v}_i \cdot \mathbf{r}_i \quad \text{where } \mathbf{r}_i \text{ is a closed loop about } \mathcal{C}_i. \quad (1.9)$$

Dimensionally, for a vortex knot of size r_f with velocity scale of U , the circulation goes as $\Gamma \sim U r_f$. In vortex dynamics the circulation Reynolds number $R_\Gamma = \Gamma/\nu$ is widely used and for a vortex knot of size r_f , the nonlinear and viscous timescales are respectively:

$$t_{NL} = r_f^2/\Gamma \quad \text{and} \quad t_\nu = r_f^2/\nu. \quad (1.10)$$

Three local densities are used. The energy density $e = \frac{1}{2}u^2$, the enstrophy density $\zeta = \omega^2$ and the helicity density $h = \mathbf{u} \cdot \boldsymbol{\omega}$. Their budget equations, with their global integrals, are:

$$\frac{\partial e}{\partial t} + (\mathbf{u} \cdot \nabla)e = -\nabla \cdot (\mathbf{u}p) + \nu \Delta e - \underbrace{\nu(\nabla \mathbf{u})^2}_{\epsilon = \text{dissipation} = \nu Z}, \quad E_e = \frac{1}{2} \int_{\mathcal{V}_\ell} \mathbf{u}^2 dV; \quad (1.11)$$

$$\frac{\partial \zeta}{\partial t} + (\mathbf{u} \cdot \nabla)|\boldsymbol{\omega}|^2 = \underbrace{2\boldsymbol{\omega} \mathcal{S} \boldsymbol{\omega}}_{\zeta_p = \text{production}} + \nu \Delta |\boldsymbol{\omega}|^2 - \underbrace{2\nu(\nabla \boldsymbol{\omega})^2}_{\epsilon_\omega = Z - \text{dissipation}}, \quad Z = \int_{\mathcal{V}_\ell} \boldsymbol{\omega}^2 dV; \quad (1.12)$$

$$\frac{\partial h}{\partial t} + (\mathbf{u} \cdot \nabla)h = \underbrace{-\boldsymbol{\omega} \cdot \nabla \Pi}_{h_f = \omega - \text{transport}} + \underbrace{\nu \Delta h}_{\nu - \text{transport}} - \underbrace{2\nu \text{tr}(\nabla \boldsymbol{\omega} \cdot \nabla \mathbf{u}^T)}_{\epsilon_h = \mathcal{H} - \text{dissipation}}, \quad \mathcal{H} = \int_{\mathcal{V}_\ell} \mathbf{u} \cdot \boldsymbol{\omega} dV. \quad (1.13)$$

Note that $\Pi = p - \frac{1}{2}\mathbf{u}^2 \neq p_h$ and is not the pressure head $p_h = p + \frac{1}{2}\mathbf{u}^2$.

In this paper the primary norms are related to the energy and enstrophy equations. Besides the dissipation rate $\epsilon = \nu Z$ (underscore in 1.11), these two viscosity-based rescalings of the enstrophy Z , (1.1) will be used:

$$\sqrt{\nu}Z(t) \quad \text{and} \quad B_\nu(t) = 1/(\sqrt{\nu}Z(t))^{1/2} = (\nu^{1/4}\mathcal{O}_{V_1})^{-1}, \quad (1.14)$$

where \mathcal{O}_{V_1} is the first volume-integrated vorticity moment (1.1). The helicity budget is included because the helicity density h is mapped onto the vorticity isosurfaces for potential comparisons with the isosurfaces of the three-fold symmetric trefoils (Kerr 2023), where its budget equation is discussed in detail.

Under $\nu \equiv 0$ Euler, both E_e (1.11) and \mathcal{H} (1.13), the global helicity, are conserved. With the pressure gradients affecting only their local Lagrangian densities e and h . In contrast, the global enstrophy Z (1.12) is not an invariant, but grows in figure 2 due to vortex stretching, as discussed in section 2.1. E_e and Z can be recast in terms to the first two Sobolev norms, H^0 and H^1 , as defined below (1.19). Due to vortex stretching, initially all H^s , $s > 1$, tend to grow.

1.2. Norms and inner products

The mathematical analysis in the appendices uses Sobolev inner products and norms. These are formed from the Fourier-transformed components $\hat{\mathbf{v}}(\mathbf{k})$ of the velocity field $\mathbf{v}(\mathbf{x})$ in a $(2\ell\pi)^3$ domain, with the wavenumbers $\mathbf{k} = \ell^{-1}\mathbf{n}$ written using three-dimensional integer vectors \mathbf{n} . Giving this definition and equation for $\hat{\mathbf{v}}_{\mathbf{k}}$

$$\mathbf{v}(\mathbf{x}) = \sum_{\mathbf{k}} \hat{\mathbf{v}}_{\mathbf{k}} e^{i\mathbf{k} \cdot \mathbf{x}}; \quad \frac{d}{dt} \hat{\mathbf{v}}_{\mathbf{k}}(t) = -\nu|k|^2 \hat{\mathbf{v}}_{\mathbf{k}}(t) - i\mathbf{P}(\mathbf{k}) \sum_{\mathbf{k}' + \mathbf{k}'' = \mathbf{k}} \hat{\mathbf{v}}_{\mathbf{k}'}(t) \cdot \mathbf{k}'' \hat{\mathbf{v}}_{\mathbf{k}''}(t) \quad (1.15)$$

The projection factor operator $\mathbf{P} = \mathbf{I} - \mathbf{k} \otimes \mathbf{k}/k^2$ incorporates the pressure in Fourier space.

The inner products come from multiplying the active equation by a test function, usually a velocity, in either real or Fourier space. Then integrating that over all space. This paper uses s -order $\dot{H}^s = \dot{H}_{2\pi}^s$ inner products that in a $\ell = 1$, $V_1 = (2\pi)^3$ domain are determined by the power of $|k|^{2s}$ used:

$$\langle u, v \rangle_s = \int_{\mathcal{V}_1} |\nabla^s \mathbf{u}(\mathbf{x}) \cdot \nabla^s \mathbf{v}(\mathbf{x})| d^3x = (2\pi)^3 \sum_{\mathbf{k}} |k|^{2s} |\hat{\mathbf{u}}_{\mathbf{k}}(t) \cdot \bar{\hat{\mathbf{v}}}_{\mathbf{k}}(t)|. \quad (1.16)$$

An inner product is a norm when $\mathbf{v} = \mathbf{u}$ with $\langle u, u \rangle_s = \|u\|_{\dot{H}^s}^2$, with this further definition: $\|u\|_s^2 := \|u\|_{\dot{H}^s}^2$.

The Navier-Stokes Fourier equation of the inner product of the $s = 0$ norm $\|u\|_0^2$ is particularly simple. Due to incompressibility, and by using integration by parts to remove the pressure, this inner product equation reduces to:

$$\frac{d}{dt} \frac{1}{2} \sum_{\mathbf{k}} |\hat{\mathbf{u}}_{\mathbf{k}}(t)|^2 = -\nu \sum_{\mathbf{k}} |\mathbf{k}|^2 |\hat{\mathbf{u}}_{\mathbf{k}}(t)|^2 \quad \Rightarrow \quad \frac{d}{dt} \frac{1}{2} \|u\|_0^2 = -\nu \|\nabla u\|_0^2 = -\nu \|u\|_1^2 \quad (1.17)$$

This set of equations demonstrates the simplification provided by taking inner products, with the discussion in sections A.1 to A.6 using the form on the right.

The ℓ -domain 2nd-order s , H_ℓ^s Sobolev norms of u , v and $w = v - u$ (1.6) can be defined using the $L_\ell^{(2)}$ and the \dot{H}_ℓ^s norms as

$$\|u_\ell\|_s^2 = \|u\|_{H_\ell^s}^2 = \|u\|_{L_\ell^{(2)}}^2 + \|u\|_{\dot{H}_\ell^s}^2 \quad (1.18)$$

where $\|u\|_{L_\ell^{(2)}}^2 = \ell^{-3} \int |u|^2 dx$ is the $\|u\|_0^2$ inner product in a $(2\ell\pi)^3$ domain and the \dot{H}_ℓ^s norms are:

$$\dot{H}_\ell^s = \|u_\ell\|_s^2 = \|u\|_{\dot{H}_\ell^s}^2 = (2\pi)^3 \ell^{3-2s} \sum_{\mathbf{k} \in \mathbb{Z}^3} |\mathbf{k}|^{2s} |\hat{\mathbf{u}}(\mathbf{k})|^2 = \ell^{3-2s} \|\nabla^s u\|^2, \quad (1.19)$$

In the appendices, for the higher-order s norms, inequalities typically replace equalities like those in (1.17) and from this point onwards, all inner products are assumed to be $L_\ell^{(2)}$ and the upper s superscript will refer to the \dot{H}_ℓ^s inner products and norms.

The physical dimensions of the velocity norms, including the volume, are: $\text{Dim}[\|u\|_s] = [\mathcal{L}^{5/2-s}/T]$ for a chosen length scale \mathcal{L} and time scale T .

1.3. Mathematics for large $(2\ell\pi)^3$ domains

A potential drawback of using periodic domains of any size is that there is a set of $(2\pi)^3$ mathematical bounds from applied analysis of the Navier-Stokes equations (Constantin 1986) that are largely unknown to the general fluid dynamics community that, with further theorems, restrict the growth of the enstrophy as ν decreases.

What was shown was that the growth all higher-order Sobolev norms under $\nu \neq 0$ Navier-Stokes are controlled by integrals of equivalent $\nu \equiv 0$ Euler norms as the viscosities become very small. More precisely, from $\nu \equiv 0$ Euler solutions $u(t)$, Analytic critical viscosities ν_s can be determined from time-integrals of the higher-order $s \geq 5/2$, Sobolev norms $H^s(u)$. These in turn control the growth of the equivalent $H^s(v)$ of $\nu_s \geq \nu \neq 0$ Navier-Stokes solutions $v(t)$.

From there, additional embedding theorems (Robinson *et al.* 2016) can then be used to show that the dissipation rate $\epsilon = \nu Z \rightarrow 0$ (1.11), unless there are singularities of either the Navier-Stokes or Euler equations. Simplified, the steps are to take the bounds upon the $H^s(v)$, apply them to embedding theorems that can bound $\|\omega\|_\infty$, from which the vorticity moment hierarchies will bound \mathcal{O}_{V_1} (1.1), Ω_1 (1.8) and Z (1.12), from which $\epsilon = \nu Z \rightarrow 0$ as $\nu \rightarrow 0$ follows. This result is not relevant when, $\nu > \nu_s$, that is if the viscosity is above the critical values ν_s .

Those results would apply to the evolution of all initial value (Cauchy) calculations done in strictly $(2\pi)^3$ domains and explain why very small ν , $(2\pi)^3$ calculations consistently fail to generate evidence for a dissipation anomaly with finite ΔE_ϵ (1.2), which is applicable to many calculations besides those cited in Yao & Hussain (2022).

The appendices here modify those $(2\pi)^3$ results for larger $(2\ell\pi)^3$ domains and show that the suppression can be mitigated by doing small ν calculations in ever larger periodic domains because the viscosity-based ν_s bounds upon the growth of vorticity moments decrease as the domain parameter ℓ increases to accommodate decreasing ν .

The basic elements of the proof will follow a recent alternative to the classic result of Constantin (1986) given in Chapter 9 of Robinson *et al.* (2016). The revisions of the original 1986 proof fill in many gaps with essential details that did not appear until Constantin & Foias (1988). One of these is a robustness proof that is then inserted where needed into the final proof. The appendices here then rescale the $(2\pi)^3$ results by assuming that the timescales and Reynolds numbers are invariant as the $\mathcal{L} = 2\ell\pi$, $(\mathcal{L})^3$ domains are increased. Finally, rather than just saying that certain very small critical viscosities exist, assumptions are made that suggest their magnitudes.

1.4. Trefoil initial condition and numerics

The trefoil vortex knot in this paper at $t = 0$ is defined as follows:

1) $\boldsymbol{\xi}_0(\phi) = [x(\phi), y(\phi), z(\phi)]$ defines the centreline trajectory of a closed double loop over $\phi = 1 : 4\pi$ with $a = 0.5$, $w = 1.5$, a characteristic size of $r_f = 2$ and a perturbation of $r_1 = 0.25$.

$$\begin{aligned} x(\phi) &= r(\phi) \cos(\alpha) \\ y(\phi) &= r(\phi) \sin(\alpha) & z(\phi) &= a \cos(\alpha) \\ \text{where } r(\phi) &= r_f + r_1 a \cos(\phi) + a \sin(w\phi + \phi_0) \\ \text{and } \alpha &= \phi + a \cos(w\phi + \phi_0) / (wr_f) \\ \text{with } t_{NL} &= r_f^2 / \Gamma = 8 \text{ the nonlinear timescale} \\ \text{and } r_e &= (\Gamma / (\pi\omega_m))^{1/2} \text{ the effective radius.} \end{aligned} \quad (1.20)$$

2) The vorticity profile $|\omega(\rho)|$ uses the distance ρ between a given mesh point \boldsymbol{x} and the nearest point on the trajectory $\boldsymbol{\xi}_0(\phi)$: $\rho = |\boldsymbol{x} - \boldsymbol{\xi}_0(\phi)|$. The profile used here is algebraic (1.21)

$$\omega_{\text{raw}}(\rho) = \omega_o \frac{(r_o^2)^{p_r}}{(\rho^2 + r_o^2)^{p_r}}. \quad (1.21)$$

with a power-law of $p_r = 1$, a radius of $r_o = 0.25$ and a centreline vorticity before projection of $\omega_o \approx 1.26$. This profile is mapped onto the Cartesian mesh, is made incompressible as described previously (Kerr 2018a), and for algebraic profiles, the $\rho < \rho_+$ map is independent of the outer ρ_+ radius (Kerr 2023). The final ω_o is chosen in each case so that the circulation is always $\Gamma = 0.505$ (1.9) and $\|\omega(0)\|_\infty = 1$, with the initial enstrophy $Z_0 = Z(t = 0) \approx 5.30$.

All of the calculations in this paper use this initial condition with different domain sizes and different mesh sizes as given in the table 1. Including the curves in figures 2 to 6.

The numerical method is the high-wavenumber filtered 2/3rds-dealiased pseudo-spectral code used previously (Kerr 2013a). However, by filtering out the ubiquitous high wavenumber tail-up, one loses a simple tool for determining whether the smallest scales are resolved by observing that tail-up.

So alternative resolution diagnostics are needed. Comparisons between calculations with different resolutions is one choice, and has been applied to the $\nu = 6.25 \times 10^{-5}$ calculations, with all of the $\Omega_m(t)$ moments for both 1024^3 calculations, that is for both $(4\pi)^3$ and $(6\pi)^3$, agreeing with those of the 2048^3 , $(4\pi)^3$ calculation. For larger Reynolds numbers, whether the resolution is adequate is determined by these diagnostics: That the $\nu^{1/4} \mathcal{O}_{V_m}$ moments converge at their respective t_m times with the lower Reynolds number calculations. This is discussed further in section 2.2 using figure 5. And by their high wavenumber spectra, as in figure 9d, where the $Z_V(k) \sim k^{-1}$ power laws bend further into viscous exponential regimes.

On the basis of those diagnostics, the small-scales of all of large ν , 1024^3 calculations and the 2048^3 calculations for the first factor of 25 decrease in ν , to $\nu = 2.2 \times 10^{-5}$, are

resolved for all times. This includes the section 4 graphics from the $\nu = 3.125 \times 10^{-5}$ calculation with the higher vorticity isosurfaces during reconnection ($t = 42$ and 48) showing vortices curling around local axes.

Nonetheless, enstrophy based results for some larger Reynolds numbers with $\nu < 2.2 \times 10^{-5}$ calculations are included. For very early times the convergence of $\nu^{1/4}\Omega_\infty(t)$ and $\nu^{1/4}\mathcal{O}_{V_9}(t)$ at $t_\infty = 18.4$ and $t_9 = 19.1$ for all ν are shown in figure 5, providing a clear sign that these $\nu < 2.2 \times 10^{-5}$ calculations are resolved for $t \lesssim 20$. And results for the enstrophy $Z(t)$ and $\mathcal{O}_{V_1}(t)$ from three smaller ν calculations in large meshes are included in figures 2b and 4. These are for $\nu = 1.56 \times 10^{-5}$, 7.8×10^{-6} and 4×10^{-6} . They are included in the sense of large-eddy simulations, with the filtering providing the subgrid dissipation. One justification is that all of the previous (Kerr 2018b) results using 1024^3 meshes have now been confirmed using 2048^3 meshes. Implying that the same should be true for at least the new $\nu = 1.56 \times 10^{-5}$ and $\nu = 7.8 \times 10^{-6}$, 2048^3 results when re-run on 4096^3 meshes.

2. Vorticity moment scaling with powers of the viscosity ν

Figure 2 introduces the unexpected (circa 2018) convergence of $\sqrt{\nu}Z(t)$ (1.14), a *reconnection-enstrophy*. With $\ell > 1$ larger $(2\ell\pi)^3 > (2\pi)^3$, domains used to ensure temporal convergence at a fixed time $t_x \approx 40$ as the viscosity ν decreases. Using the \mathcal{O}_{V_1} (1.1), Kerr (2018a) found that the best way to observe this convergence was to plot $B_\nu(t) = (\nu^{1/4}\mathcal{O}_{V_1})^{-1} = 1/(\sqrt{\nu}Z(t))^{1/2}$ (1.14), discussed here in section 2.1 where $t_x \approx 40$ is taken to be when the reconnection phase ends. As defined by the graphics in section 4.

In 2018, it was noted that the ν -independent convergence of $\sqrt{\nu}Z(t)$ seemed contrary to an analytic result from Constantin (1986). Kerr (2018b) suggested that an analytic extension of that old result might exist, which is now described in the appendices.

Two simulations with $\nu = 3.1 \times 10^{-5}$ in figure 2 illustrate what happens if the domain is not increased as ν decreases. The brown+ curve, done in a $\ell = 2$, $(4\pi)^3$ domain passes below $\sqrt{\nu}Z = 0.15$ at $t = 40$. The green Δ curve was done in a $\ell = 3$, $(6\pi)^3$ domain and passes through $\sqrt{\nu}Z = 0.15$ at $t = 40$, which implies that in a $(4\pi)^3$ domain, the empirical critical viscosity for this initial condition is $\nu_c \sim 3.1 \times 10^{-5}$.

To maintain the $\sqrt{\nu}Z(t)$ convergence as the viscosity ν is decreased and the Reynolds number is increased further, ν_c had to be decreased by increasing the domain parameter ℓ repeatedly (Kerr 2018a,b). This practice was continued several times, showing empirically that the critical length scale ℓ_c depends upon ν as, or critical viscosity ν_c depending upon the length scale ℓ as:

$$\ell_c \sim \nu^{-1/4}, \quad \text{or} \quad \nu_c \sim \ell^{-4}. \quad (2.1)$$

Raising this question: what is origin of the dependence of the empirical critical viscosities $\nu_c(\ell)$ upon ℓ and $\nu^{-1/4}$? Section 2.2 discusses the ubiquitous nature of the $\nu^{1/4}$ scaling, with the appearance of double vortex sheets in section 4 seeming to underlying the dynamics. However, trefoils are too complicated to be able to see the underlying dynamics clearly, so alternative configurations such orthogonal vortices are being used, with the preliminary conclusion summarised in section 6 being:

- The usual $\sqrt{\nu}$ scaling does appears as the double sheets are being pushed together.
- Balanced by $\ell \sim \nu^{-1/4} = (\sqrt{\nu})^{-1/2}$ scaling developing at their outer edges as the sheets spread out.

Note that the convergence of $\sqrt{\nu}Z(t)$ as ν decreases is not convergence of the energy dissipation rate $\epsilon = \nu Z$, which comes later, for $t > t_x$, as the post-reconnection enstro-

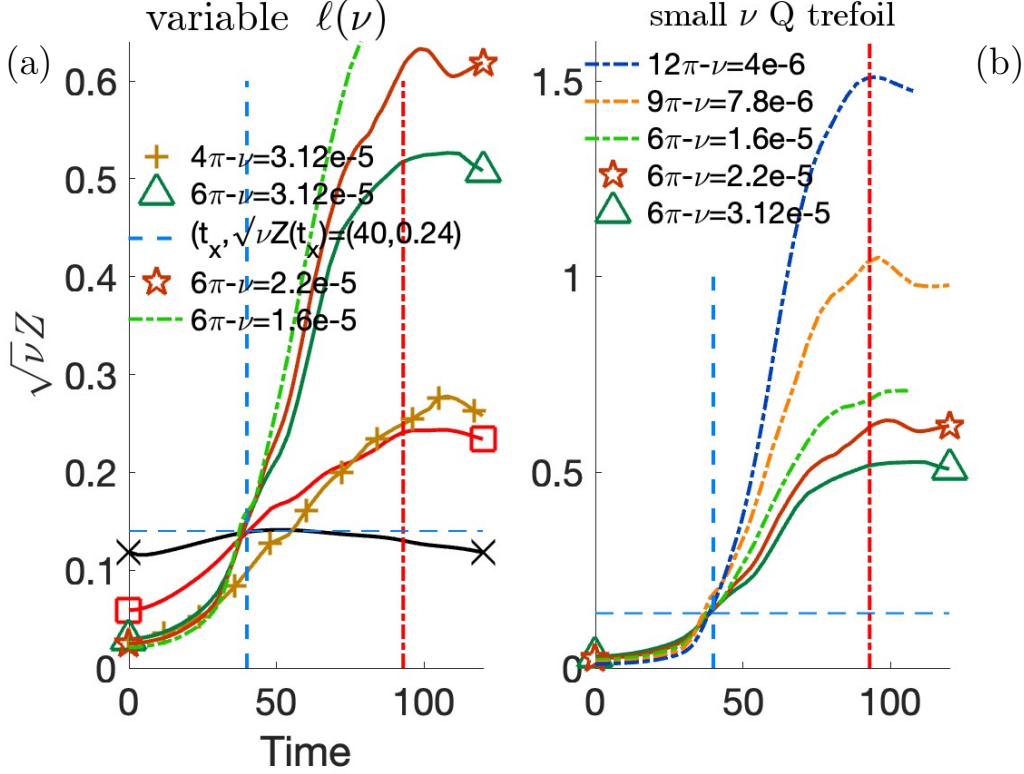


FIGURE 2. Time evolution of the *reconnection enstrophy* $\sqrt{\nu}Z(t)$ with all crossing at $t = t_x = 40$ with $\sqrt{\nu}Z(t_x) = 0.14$. The lower $\nu \leq 3.125 \times 10^{-5}$ viscous cases were given previously (Kerr 2018b) with $t_x = 40$ identified as the end of the reconnection phase. The line at $t_\epsilon = 93$ is when plots of the dissipation $\epsilon = \nu Z$ approximately cross in figure 4. (a) The brown-+ curve is from a $\nu = 3.125 \times 10^{-5}$, $(4\pi)^3$ calculations, the same domains as the lower $\nu < 3.125 \times 10^{-5}$ viscous cases, but $\sqrt{\nu}Z(t = 40) \neq 0.14$. Unlike the $\nu = 3.125 \times 10^{-5}$ green curve that was run in a $(6\pi)^3$ domain, with $\sqrt{\nu}Z(40) = 0.14$, plus a resolved $\nu = 2.2 \times 10^{-5}$ case (dark-red \star). (b) Along with the two highest Reynolds number $(6\pi)^3$, resolved calculations, $\nu = 3.125 \times 10^{-5}$ (green-triangle) and $\nu = 2.21 \times 10^{-5}$ (dark-red \star), three under-resolved higher Reynolds number, $\nu < 2.21 \times 10^{-5}$ cases show continuing convergence of $\sqrt{\nu}Z(t)$ at $t = t_x = 40$ as well as strong peaks at $t_\epsilon \approx 93 \approx 2t_x$.

phy growth accelerates. Unlike the similarity-like growth of the higher-order vorticity moments described next, similar convergence of $\epsilon(t) = \nu Z$, around a given time should not be expected. Instead there is approximate convergence of $\epsilon(t) = \nu Z$ that begins at $t \sim 70$ with peaks at $t_\epsilon \approx 2t_x$ in figure 4, with associated spectra that are discussed in section 3.

2.1. Reconnection phase scaling $(\sqrt{\nu}Z)^{-1/2} = (\nu^{1/4}\mathcal{O}_{V1})^{-1}$

In this subsection, figures 3 and 4 use these two alternative viscous rescalings of $Z(t)$ (Kerr 2018b), $B_\nu(t) = 1/(\sqrt{\nu}Z(t))^{1/2} = (\nu^{1/4}\mathcal{O}_{V1})^{-1}$ (1.14) and $\epsilon(t) = \nu Z(t)$ (1.11) respectively. Since originally introduced (Kerr 2018a), convergent, inverse linear $B_\nu(t)$ regimes have been found for the interaction of coiled vortex rings (Kerr 2018c), three-fold symmetric trefoils (Kerr 2023) and additional configurations discussed in section 5.1.

The extensions in figure 3 come from linearising $B_\nu(t)$ about ν -independent $B_x = B_\nu(t_x) \approx 2.67$ and extending each linear $B_\nu(t)$ over $t \lesssim t_x$ ($30 \leq t \leq 40$) to define

$\tilde{\nu}(\times 10^{-4})$	5	2.5	1.25	0.625	0.625	0.312	0.312	0.22	0.16	0.078	0.04
Domain	$(4\pi)^3$	$(4\pi)^3$	$(4\pi)^3$	$(4\pi)^3$	$(6\pi)^3$	$(6\pi)^3$	$(6\pi)^3$	$(6\pi)^3$	$(6\pi)^3$	$(9\pi)^3$	$(12\pi)^3$
Adequate?	good	good	good	good	good	not	good	good	good	good	good
Mesh	1024^3	1024^3	1024^3	1024^3	2048^3	1024^3	2048^3	2048^3	2048^3	2048^3	2048^3
Resolved?	yes	yes	yes	yes	yes	yes	yes	yes	no	no	no
Symbols	X	*	□	○	⊗	+	△	*	--	--	--
Colours	black	blue	red	magenta	purple	brown	green	maroon	lime	orange	cobalt

TABLE 1. Perturbed trefoil cases parameters. Rows: $\tilde{\nu} = \nu \times 10^4$. Domain?: Is the computational domain large enough based upon ℓ_c (2.1)? Computational Mesh, with 2048^3 for $\nu = 6.25 \times 10^{-5}$ to $t = 48$ and 1024^3 to $t = 192$. Resolved?: Does this mesh resolve the flow?? Symbols. Colours.

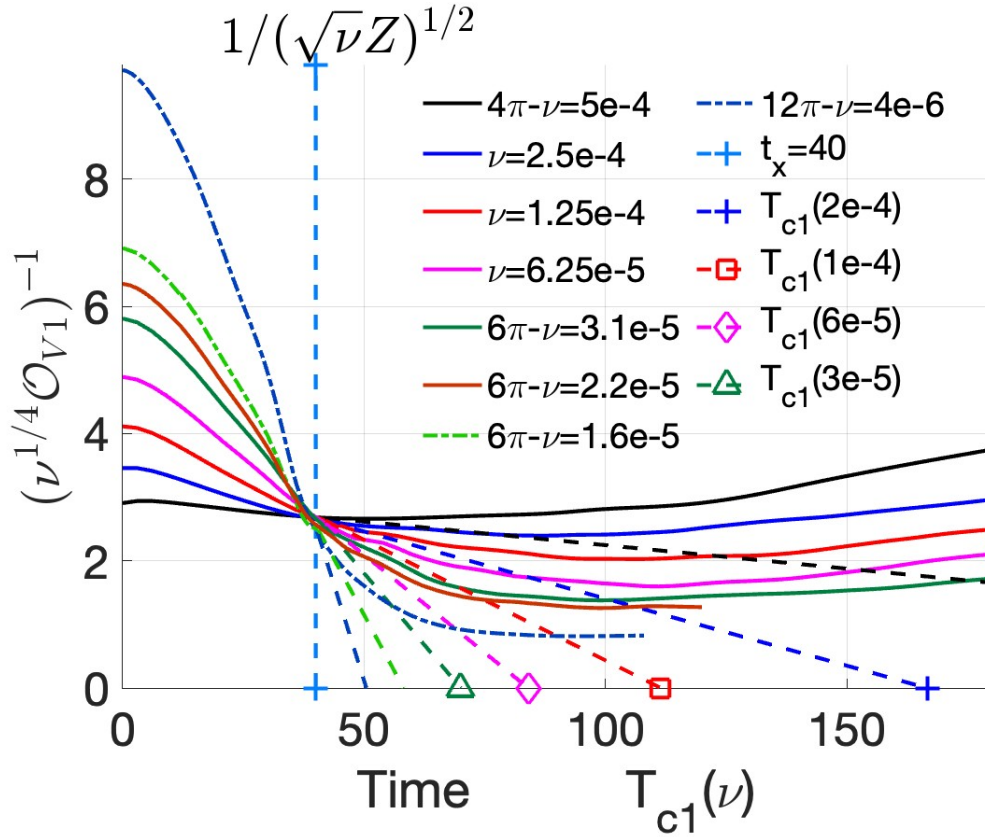


FIGURE 3. This and the next figure show further viscosity-based rescalings of the enstrophy Z . Here, using inverse $(\sqrt{\nu}Z)^{-1/2}$ scaling, rewritten as $(\nu^{1/4} \mathcal{O}_{V1})^{-1}$, shows ν -independent inverse-linear convergence at $t = t_x = 40$. To emphasise that the convergence is inverse linear, $t > t_x$ extensions of the $t \lesssim t_x$ behaviour are shown using long-dashed lines. Empirically, increases in the domain sizes $(2\ell\pi)^3$, with $\ell(\nu) \sim \nu^{-1/4}$, are required to maintain the $t \lesssim t_x$ linear scaling as ν decreases. The $t > t_x$ linear extensions to $T_c(\nu)$ are given by (2.2).

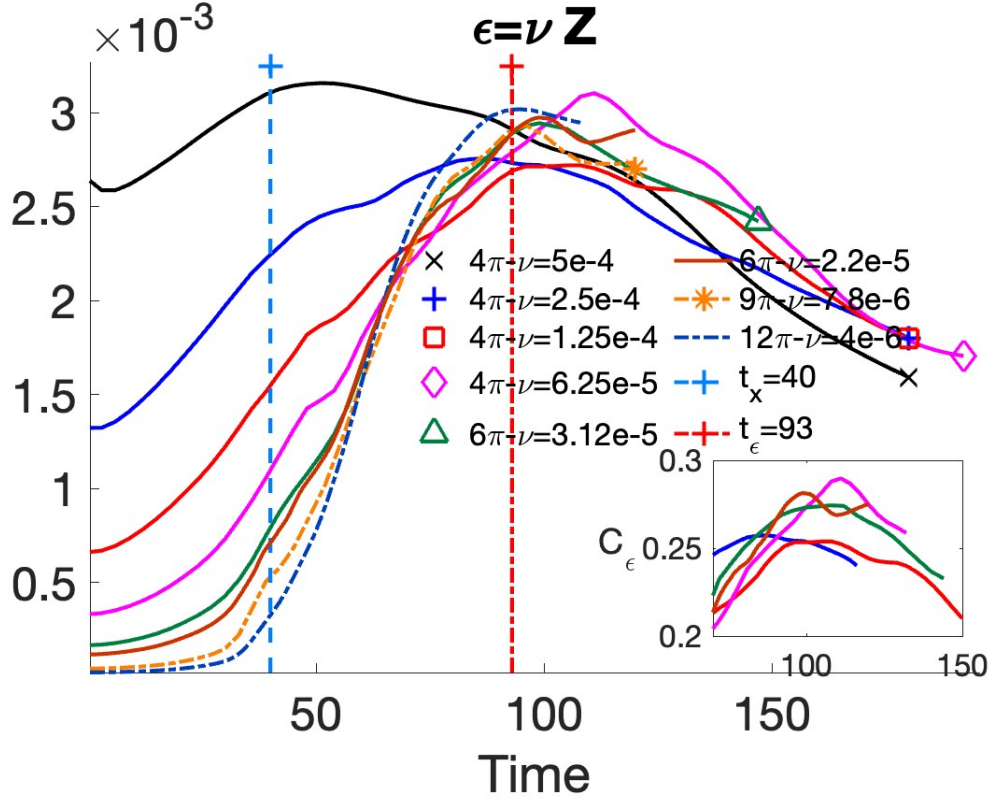


FIGURE 4. The dissipation rate $\epsilon = \nu Z$ for seven cases, $\nu = 5 \times 10^{-4}$ to 4×10^{-6} , showing approximate convergence of the dissipation rates beginning at $t \sim 70$, with peaks at $t_\epsilon \approx 93 \approx 2t_x$, that continues for an extended period. These trends are consistent with the formation of a *dissipation anomaly*, that is finite energy dissipation ΔE_ϵ (1.2) in a finite time as ν decreases. Inset: ϵ rescaled as the dissipation coefficient C_ϵ (1.3) using $\mathcal{L} = 2r_f = 4$ and $\mathcal{U} = \|u\|_\infty(t_\epsilon = 93) \approx 0.34$ for calculations whose maximum Taylor microscale Reynolds number at $t = 93$ is $R_\lambda = 218$.

$T_c(\nu) > t_x$ as when $t > t_x$ inverse linear $B_\nu(T_c(\nu)) = 0$. The purpose of identifying these $t > t_x$ linear extensions is to emphasize the inverse linearity of the pre- t_x $B_\nu(t)$, which suggests some type of self-similar process that might be found.

Specifically for $t_{30} = 30$ and $t_x = 40$ and using

$$\Delta t(\nu) = B_x \frac{t_x - t_{30}}{B_\nu(t_{30}) - B_x} \quad \text{and} \quad T_{c1}(\nu) = t_x + \Delta t(\nu) \quad (2.2)$$

one gets for these viscosities: $\nu = [0.5 \ 0.25 \ 0.125 \ 0.0625 \ 0.0312 \ 0.0156 \ 0.004] \times 10^{-3}$, these $\Delta t(\nu) = [364 \ 127 \ 71.5 \ 44.1 \ 30 \ 18.2 \ 10.5]$ and these $T_{c1} = [403.9 \ 166.6 \ 111.5 \ 84.1 \ 70.0 \ 58.2 \ 50.5]$.

Kerr (2018b) used the linearity for $t \lesssim t_x$ to show how to collapse the $B_\nu(t)$ onto one another in a ν -independent manner. This suggested that an underlying scaling process exists with a role for the double square-root on the viscosity. That is scaling using $\nu^{1/4}$ (1.14). The next section will follow this up by extending the \mathcal{O}_{V1} scaling to higher order \mathcal{O}_{Vm} and section 6 will begin by mentioning other configurations with this scaling.

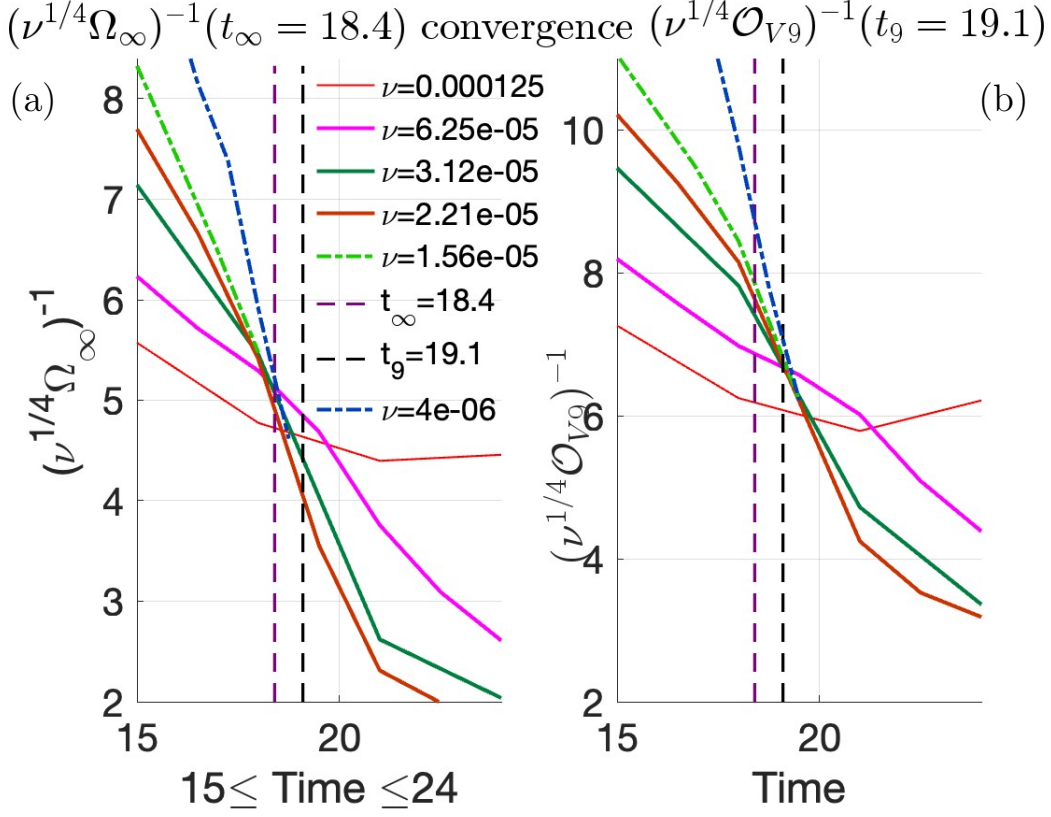


FIGURE 5. (a) $(\nu^{1/4}\Omega_\infty)^{-1}$ and (b) $(\nu^{1/4}\mathcal{O}_{V9})^{-1}$. Recall that the end of the reconnection phase is indicated by when the $\sqrt{\nu}Z(t)$ converge at $t_x = 40$ in figure 3. For $\nu = 6.25 \times 10^{-5}$ to $\nu = 4 \times 10^{-6}$, in (a) the $(\nu^{1/4}\Omega_\infty(t))^{-1}$ converge at $t_\infty \sim 18.4$ and in (b) the $(\nu^{1/4}\mathcal{O}_{V9})^{-1}$ converge at $t_9 \sim 19.1$.

2.2. Additional $\nu^{1/4}$ scaling examples.

Figure 5 shows inverse $\nu^{1/4}$ scaling of $\Omega_\infty(t)$ and $\mathcal{O}_{V9}(t)$ (1.1): $(\nu^{1/4}\Omega_\infty(t))^{-1}$ and $(\nu^{1/4}\mathcal{O}_{V9}(t))^{-1}$, recalling that at $t = 0$ $\Omega_\infty = \|\omega\|_\infty = 1$ is imposed.

Figure 5a shows that the ν -independent temporal convergence of $(\nu^{1/4}\Omega_\infty(t))^{-1}$ is at $t_\infty = 18.4$ and figure 5b shows this for $(\nu^{1/4}\mathcal{O}_{V9}(t))^{-1}$ at $t_9 = 19.1$. For both, their temporal convergences at t_∞, t_9 are best for $\nu = 6.25 \times 10^{-5}$ to 4×10^{-6} , with the thin $\nu = 1.25 \times 10^{-4}$ curves at too low a Reynolds number to be fully included. For the dot-dash $\nu < 2.2 \times 10^{-5}$ cases, the resolution is adequate only up to $t \sim 19$, but inadequate after that for the highest-order moments.

The convergences of these large m , $\nu^{1/4}\mathcal{O}_{V_m}$ provide the earliest quantitative evidence that the size of the domain is affecting vorticity growth. That is, a sign that the local growth of $\Omega_\infty = \|\omega\|_\infty$ (and \mathcal{O}_{V9}) is being affected by interactions across the periodic boundaries, interactions that can be suppressed if the periodic domains increase as $\ell \sim \nu^{-1/4}$ as ν decreases. The $t \lesssim t_m$ evolution of all the $(\nu^{1/4}\mathcal{O}_{V_m}(t))^{-1}$ are approximately inverse-linear, similar to how $(\nu^{1/4}\mathcal{O}_{V1}(t))^{-1}$ behaves in figure 3. Note that both t_∞ and t_9 are at $\approx t_x/2$.

Can this early time evolution of $\nu^{1/4}\Omega_\infty(t)$ and $\nu^{1/4}\mathcal{O}_{V9}(t)$ tell us anything about the

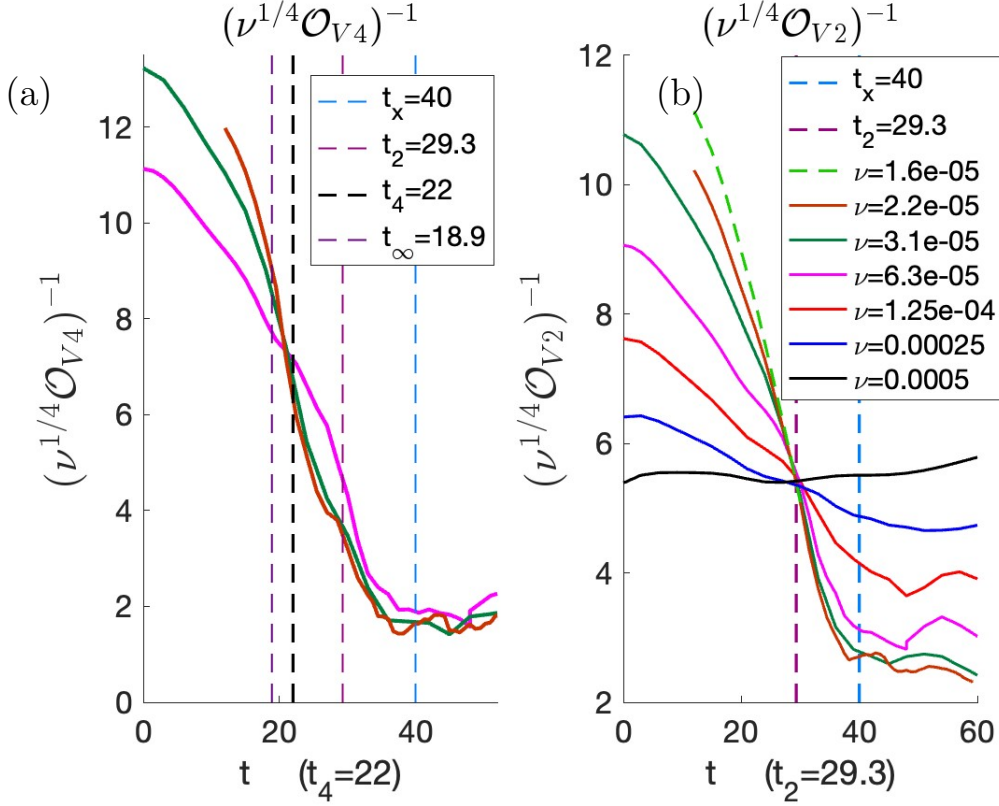


FIGURE 6. (a) $\nu^{1/4}\mathcal{O}_{V4}$ for $t \leq 50$. Recall that $t_1 = t_x = 40$ is the end of the reconnection phase. Also marked are $t_2 \sim 29.3$, $t_4 \sim 22$ and $t_\infty \sim 18.4$ with $t_x > t_2 > t_4 > t_\infty$. (b) $\nu^{1/4}\mathcal{O}_{V2}$ for $t \leq 60$ with $\nu = 1.56 \times 10^{-5}$ converging at $t_2 = 29.3$.

origins of the $\nu^{1/4}$ scaling? For that a physical model is needed, such as understanding of the origin, extent and scaling of vortex sheets like those in figures 10 and 11. But first, let us consider the evolution of the intermediate vorticity moments, $\mathcal{O}_{V_m}(t)$.

For all orders m there is convergence of $\nu^{-1/4}\mathcal{O}_{V_m}^{-1}$ at their respective t_m , ordered as $t_\infty < \dots < t_m \dots t_1 = t_x$, with ν -independent $\sqrt{\nu}Z(t_x)$ above all others. Figure 6 shows two of these intermediate scaled, inverse moments. $\nu^{-1/4}\mathcal{O}_{V4}^{-1}$ and $\nu^{-1/4}\mathcal{O}_{V2}^{-1}$. For $\nu^{-1/4}\mathcal{O}_{V4}^{-1}$ from $\nu = 6.25 \times 10^{-5}$ to $\nu = 1.56 \times 10^{-5}$, there is convergence at $t_4 = 22$ and for $\nu^{-1/4}\mathcal{O}_{V2}^{-1}$ for the same ν at $t_2 = 29.3$.

One way to understand the relationship between $\nu^{1/4}\Omega_\infty$ and the $m < \infty$ volume-integrated moments $\nu^{1/4}\mathcal{O}_{V_m}(t)$, including the $(\sqrt{\nu}Z)^{1/2} = (\nu^{1/4}\mathcal{O}_{V1})^2$, is to realise that $\|\omega\|_\infty = \Omega_\infty$ is point-like. Because the $t_\infty = 18.4$ convergence comes first, as ω near $\Omega_\infty(t)$ continues to grow, the region with $\omega \sim \|\omega\|_\infty$ begins to spread out, resulting in increases of the other \mathcal{O}_{V_m} , until one gets vortex sheets like those in figure 10.

To determine whether the resolution is adequate, one common diagnostic is to follow and compare values of $\|\omega\|_\infty = \Omega_\infty$, with figure 5 showing both $\nu^{1/4}\Omega_\infty(t)$ and $\nu^{1/4}\mathcal{O}_{V9}(t)$ converging at $t_\infty = 18.9$ and $t_9 = 19.1$ respectively for all ν . Furthermore, for $\nu \gtrsim 2.2 \times 10^{-5}$ and $t \geq 20$, as ν decreases the inverse $\|\omega(t)\|_\infty$ and $\mathcal{O}_{V9}(t)$ continue to decrease as expected.

However for $t > 20$, the smaller ν , $\nu < 2.2 \times 10^{-5}$, these highest-order Ω_m do not

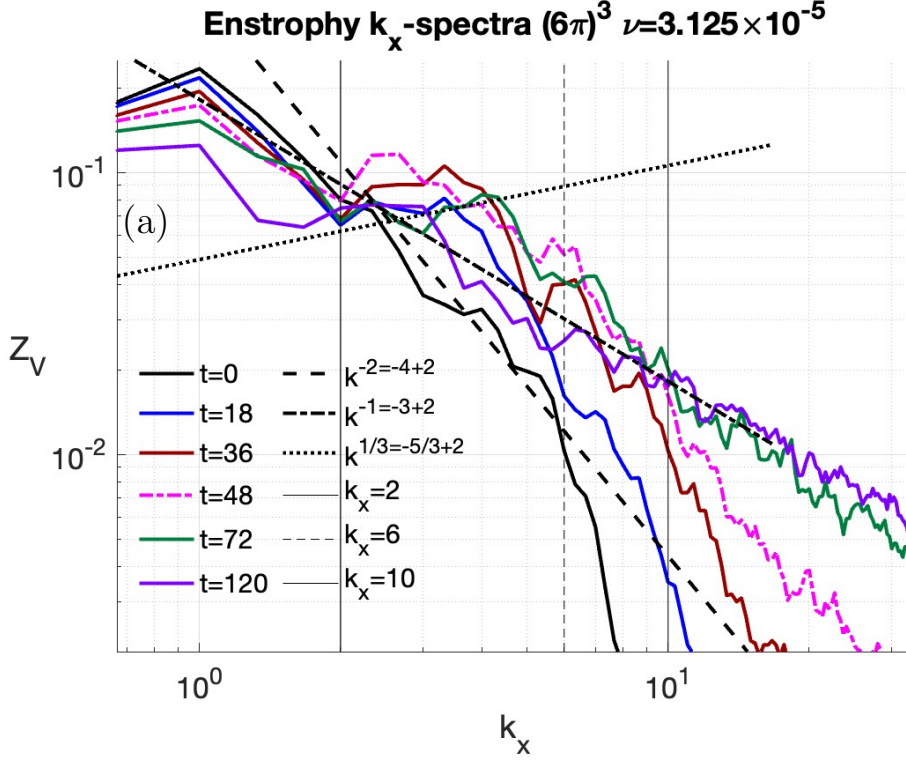


FIGURE 7. Enstrophy spectrum $Z_V(k_x)$ for seven times from the $\nu = 3.125 \times 10^{-5}$ perturbed trefoil case run in a $(6\pi)^3$ domain. Times are $t = 6, 18, 36, 48, 72, 96$ and 120 , plus three power laws, $k_x^{-5/3+2} = k_x^{1/3}$, $k_x^{-3+2} = k_x^{-1}$ and $k_x^{-4+2} = k_x^{-2}$. Due to the logarithmic k_x -scale, $k_x < 2$ values are overemphasized compared to $k_x > 2$ values. $k_x < 2$ spectra generally decrease with time, excepting $k_x = 2$ $t = 48$, as small-wavenumber energy begins its transfer to higher-wavenumbers. $k_x \geq 6$ spectra gradually grow over time until all approximately obey k_x^{-1} for all $10 \geq k_x \geq 30$.

decrease as would be expected, indicated that they are no longer fully resolved and are not shown. Leading to the conclusion that the only calculations that are adequately resolved for all times are those with $\nu \geq 2.21 \times 10^{-5} \approx 5 \times 10^{-4}/25$.

3. Dissipation and spectra

The convergence properties of the $\nu^{-1/4} \mathcal{O}_m(t)$ scaled vorticity moments just reported come from a phase when the dynamics is dominated by the emergence $h < 0$ vortex sheets, which might be indicating the emergence of a self-similar process. Can this scaling be extended to cover convergence of the dissipation rates $\epsilon(t)$?

It would be surprising if the post-reconnection vorticity moment and enstrophy evolution, that is for $t \geq t_x \sim 40$, continued this particular type of convergent scaling. Which $\epsilon(t)$ for $t \geq 40$ in figure 4 shows. Nonetheless, the set of $\epsilon(t) = \nu Z(t)$ curves in figure 4 do indicate that the growth of the post-reconnection enstrophy accelerates sufficiently to obtain approximate convergence of $\epsilon(t)$ for $t \geq 70$ up to a maxima at $t_\epsilon \sim 93 \sim 2t_x$, which then persists for a period of at least $\Delta T_\epsilon \sim t_x \searrow 0.5t_\epsilon$ at the end of these calculations. Observed both here and for the three-fold symmetric trefoils (Kerr 2023). Thus providing

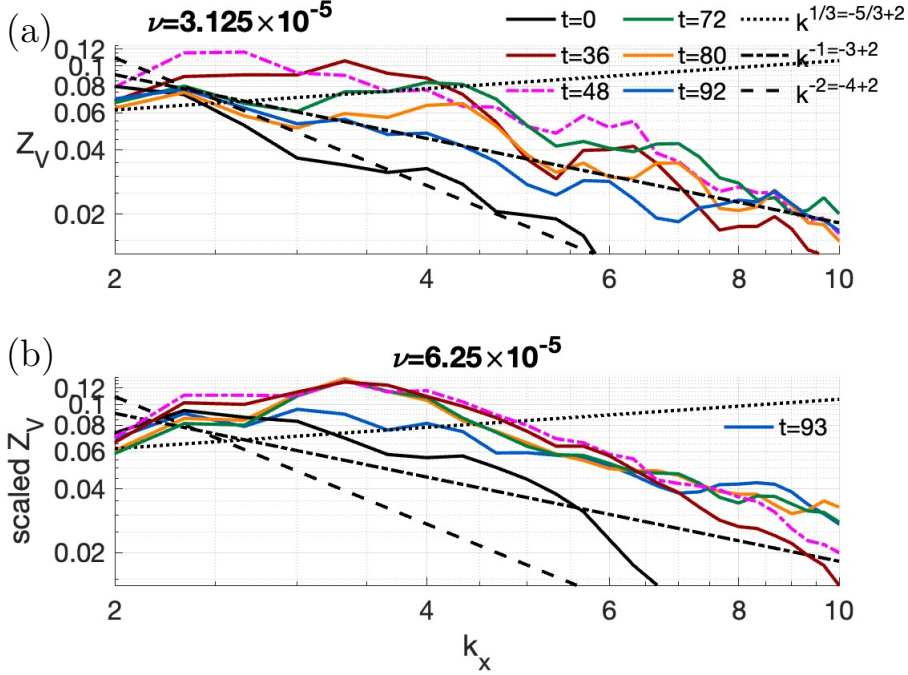


FIGURE 8. Comparisons of enstrophy spectra $Z_V(k_x)$ for two intermediate resolved Reynolds number (Re) calculations of their $t = 0$ and intermediate times ($t = 36$ to 92 or 93) for the wavenumber span $2 < k_x < 10$ to show the first step in how the enstrophy's form of Kolmogorov scaling, $Z_V(k_x) \sim k_x^{1/3}$, develops. (a) has a more thorough look at $\nu = 3.125 \times 10^{-5}$, showing that at $t = 48$ for $k_x \sim 3$, the $Z_V(k_x)$ spectrum briefly overshoots $k_x^{1/3}$, before becoming $Z_V(k_x) \sim k_x^{1/3}$ for $t = 72$ to 80 . (b) $\nu = 6.25 \times 10^{-5}$ shows that for smaller Re the spectrum also overshoots $k_x^{1/3}$, but a clear $Z_V(k_x) \sim k_x^{1/3}$ regime does not form afterwards.

evidence for finite ΔE_ϵ (1.2) and satisfying one definition for a *dissipation anomaly* with finite-time integrated energy dissipation.

Furthermore in its inset, figure 4 shows that the dissipation constant is $C_\epsilon \sim 0.25$ (1.3), values that are consistent with the range of C_ϵ from a new set of flows behind bluff bodies Schmitt *et al.* (2024), rather than the larger C_ϵ from older wind tunnel experiments that are usually reported (Vassilicos 2015).

3.1. Trefoil spectra

Turbulent flows, either forced or away from boundaries, have finite energy dissipation rates and tend to generate energy spectra with Kolmogorov scaling. And simulations of homogeneous turbulence, with some evidence for Kolmogorov scaling, can be represented by forcing the flow at small wavenumbers, starting with Kerr (1985) and now at much higher Reynolds numbers (Ishihara *et al.* 2009). The advantage that these statistically-steady data sets have is that time averages can be taken that smooth out transients.

Taking steady-state averages is not an option for the transient flows generated from configurations of reconnecting vortices. As reviewed by Yao & Hussain (2022), the only Kolmogorov-like $E(k) \sim k^{-5/3}$ spectra for a reconnection simulation comes from a brief time span with maximal enstrophy from an anti-parallel vortex calculation. And for the trefoil reviewed therein (Yao *et al.* 2021), its energy spectrum of $k^{-7/3}$ is much steeper than $k^{-5/3}$. Furthermore, for all of those cases, the time spans over which those spectral

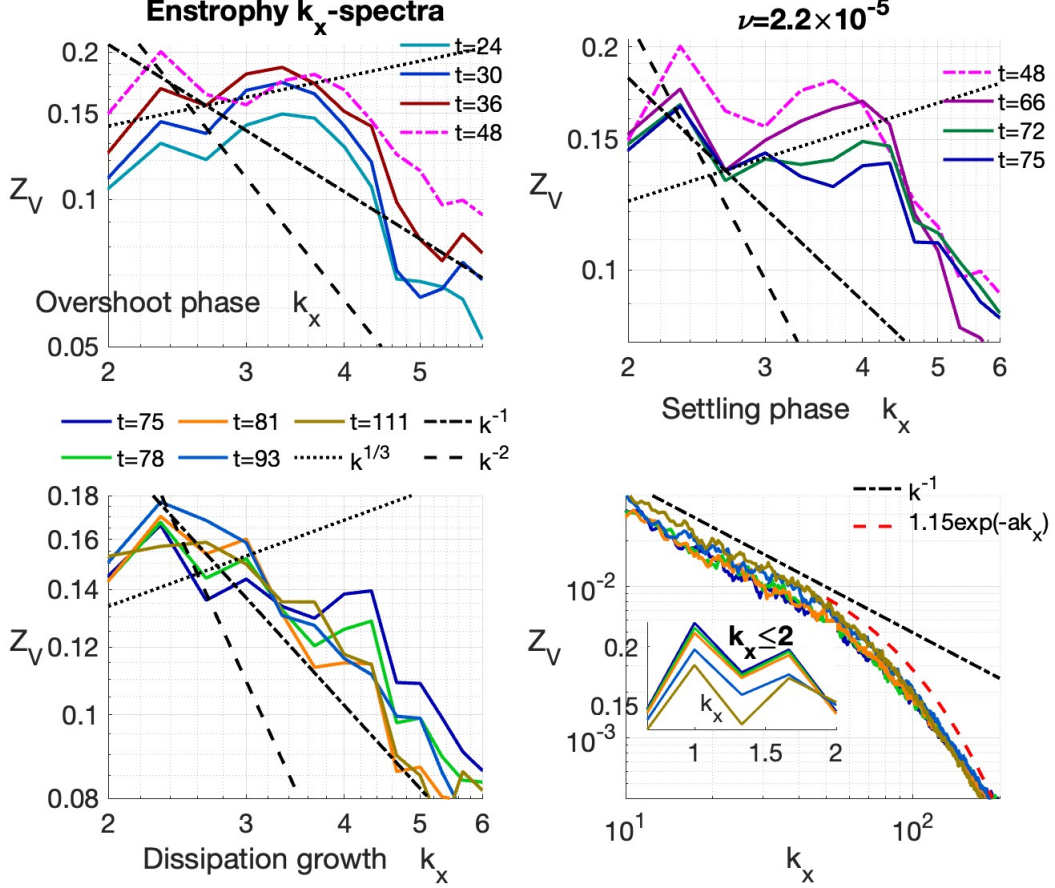


FIGURE 9. Enstrophy spectra $Z(k_x)$ for early, intermediate and late times ($t = 24$ to 111) for the highest resolved Reynolds number (Re) calculation ($\nu = 2.2 \times 10^{-5}$) run on a 2048^3 mesh. (a-c) show the wavenumber span $2 < k_x < 6$ with $t = 48$ shown in both frames (a) and (b) and $t = 75$ in (b-d). For $t \leq 36$ in (a), the spectra briefly overshoot $k_x^{1/3}$. (b) has the best evidence for approximately $k_x^{1/3}$ persisting from finite time span of $t = 66$ to 75 for $2.67 \leq k_x \leq 4.33$. Note that the leading high-wavenumber of that $k_x^{1/3}$ span increases slightly with time to $t = 75$, with this nascent $k_x^{1/3}$ span starting to decay at $t = 78$ in figure 9c. $t \sim 70$ is roughly the time when convergence of the dissipation rates $\epsilon(t)$ begins in figure 4. Both low and very high wavenumbers for $t \geq 75$ are shown in (d). At high wavenumbers there is a continuation of the $k_x \geq 5$ formation of a k_x^{-1} enstrophy spectral regime from (c) that persists until $k_x \sim 50$, with approximately exponential decay for $k_x > 50$, indicated by the rough red-dashed fit. The inset of (d) shows very low wavenumbers of $k_x \leq 2$ with those $Z_V(k_x)$ decreasing, resuming the trend shown in figure 7.

scalings were observed are too short to yield a significant decrease in the kinetic energy. For that trefoil case, this has been shown to be due to the restrictions from using the Lamb-Oseen profile (Kerr 2023).

Nonetheless, could a trefoil vortex knot with an algebraic initial profile, finite energy dissipation and temporally inhomogeneous evolution, generate energy spectra with Kolmogorov-like scaling without taking averages?

As an alternative to determining if there is Kolmogorov scaling, without statistically-steady data sets, the transient enstrophy spectra $Z_V(k)$ are followed through the wavenumber scales to show how the enstrophy grows and is transported between scales. Given that the enstrophy equivalent to $E(k) \sim k^{-5/3}$ is $Z_V(k) \sim k^{1/3}$, further questions might include how $Z_V(k)$ might overshoot $k^{1/3}$, whether there are brief $Z_V(k, t)$, sub- $k^{1/3}$ periods, how long it might maintain $k^{1/3}$ scaling, and then how $Z_V(k)$ dissipates. And if a $Z_V(k) \sim k^{1/3}$ regime does appear for a brief period, it would only be as a bonus that could lead us to a new set of refined questions.

To identify the significant temporal regimes and to facilitate comparisons over several viscosities, only $(6\pi)^3$ perturbed trefoil calculations are shown, along with several plausible comparison power laws, $k^{1/3}$, k^{-1} and k^{-2} . All wavenumbers are k_x . Figure 7 shows the progression over $t = 0$ to $t = 120$ of $Z_V(k_x, t)$ for $2/3 \leq k_x \leq 33$ from the $\nu = 3.125 \times 10^{-5}$ calculation, with these points

- $k_x < 2$ spectra generally decrease with time.
- At higher $k_x \geq 6$, there is a steady progression from the very steep $t = 0$ spectrum to $Z_V(k_x) \sim k_x^{-1}$, $E(k_x) \sim k_x^{-3}$, spectra that are discussed further using figure 9d.
- The $t = 36$ and $t = 48$ spectra overshoot the $k_x^{1/3}$ scaling.
- $t = 48$ is marked using \dashv because this represents the transition between pre- and post-reconnection scaling, after which $Z_V(k_x)$ spreads out until $t = 72$.
- $k_x^{1/3}$ scaling goes through the $t = 72$ curve for $2 \leq k_x \leq 4$ in both figures 7 and 8a, with the full $2 \leq k_x \leq 10$ behaviour in figure 8a.

Figure 8 shows the progression of $Z_V(k_x, t)$ for two viscosities from $t = 0$ to $t = 92$ or 93 for $\nu = 3.125 \times 10^{-5}$ and $\nu = 6.25 \times 10^{-5}$ respectively. For both viscosities there is growth for $t < 48$, $2 < k_x < 4$ and for $k > 6$, as t increases a k_x^{-1} regime is forming. And at both $t = 36$ and 48 for $k \sim 2.5 - 3.5$, overshooting of any $k_x^{1/3}$ scaling is developing. What is different between the two? (a) For $\nu = 3.125 \times 10^{-5}$ and $t = 72$ over $(2 \leq k \leq 4)$ there is a $Z_V \sim k_x^{1/3}$ regime, which at $t = 80$ moves to $(3 \leq k \leq 4.5)$

Figure 8(b) for $\nu = 6.25 \times 10^{-5}$ is shown to clarify how the progression of spectra appear at lower Reynolds numbers with the $k \geq 2$ spectra increasing until $t = 48$, including the growing high-wavenumber $Z_V(k_x) k_x^{-1}$ regime, which is followed by the $k_x \geq 3$ spectra tending to decay, but not uniformly and without a convincing $Z_V \sim k_x^{1/3}$ regime.

These observations raise these questions:

- How do the spectra attain approximately $Z_V(k_x) \sim k^{1/3}$ scaling?
- Does this spectrum persist long enough to attain finite energy dissipation $\Delta_\epsilon E$ (1.2)?

To begin to answer these questions, figure 9 uses four time frames from the highest Reynolds number $\nu = 2.2 \times 10^{-5}$ resolved simulation to show how a transient $Z_V(k_x) \sim k^{1/3}$ regime forms and how long it persists. Figures 9a-c all cover $2 \leq k_x \leq 6$.

- Figure 9a highlights the overshoot phase that ends between $t = 36$ and 48 .
- Figure 9b shows a settling phase with the best evidence for Kolmogorov-like scaling over a brief time span of $t = 66$ to $t = 75$ as the enstrophy spectrum settles over $2.67 \leq k_x \leq 4.33$ to $Z_V(k_x) \sim k^{1/3}$
- This is within the times $t \sim 70 - 120$ in figure 4 when there is temporal convergence of the energy dissipation rates $\epsilon(t)$ (1.11) for several viscosities, with the maxima of the $\epsilon(t)$ at $t_\epsilon \approx 93$.
- For $t \geq 75$, k_x is split into three parts as follows.
 - $k_x \leq 2$ is in the inset of figure 9d and is similar to the $t = 72$ to 120 evolution for $\nu = 3.125 \times 10^{-5}$ in figure 7, with the very largest scales (smallest k_x) still influenced by the original, now decaying, trefoil structure.
 - Figure 9c shows the influence of the high-wavenumber dissipation, with $Z_V(k_x)$ at

the largest k_x , including the $k^{1/3}$ regime, generally decaying. Again within the time span of $t \sim 70 - 120$ from figure 4 with approximately convergent energy dissipation rates $\epsilon(t)$.

- Figure 9d shows $k_x > 10$. $Z_V \sim k_x^{-1}$ from the $k_x \sim 6$ span continues to dominate for $k_x \leq 50$, followed by approximately exponential k_x -spectra for $k_x > 50$. Which is an indication that the smallest, dissipative scales of this calculation are adequately resolved.

3.2. Spectral summary

Taken together, these observations show that for this unforced calculation, by increasing the domain, a wider range of viscosities ν and Reynolds numbers Re is possible than those in Kerr (2023). A range that is wide enough to allow, beginning at $t \sim 72$, the formation of a finite-time period with convergence of $\epsilon(t) = \nu Z(t)$ and spectral scaling with a precursor to Kolmogorov scaling.

- These are properties usually associated with turbulent flows, showing that for these and the earlier Kerr (2023) calculations, these properties can form without the formation of a statistically-steady state.

- However, are these transient quasi- $k^{1/3}$ regimes consistent with the experimental observations of Kolmogorov spectra? To conclude that will require further analysis, including fully three-dimensional spectra plus energy flux and enstrophy production spectra (Kerr 1990).

4. Three-dimensional structural evolution

In this section two phases of the structural evolution of these flows are addressed. One is the $t \leq t_x \approx 40$ phase with $\sqrt{\nu}Z(t)$ convergence highlighted in figure 3. The other, is the first hints of how the vortices evolve to generate the approximate ν -independent convergence $\epsilon = \nu Z(t)$ convergence in figure 4.

For three-fold symmetric trefoils with algebraic core profiles, Kerr (2023) shows that negative helicity vortex sheets are being shed between the reconnecting vortices, unlike the localized braids and bridges that appear when Gaussian/Lamb-Oseen profiles are used, as reviewed by (Yao & Hussain 2022). The calculations in this paper all use the algebraic profile introduced for several anti-parallel Navier-Stokes and Euler calculation in 2013 (Donzis *et al.* 2013; Kerr 2013a,b), plus some analysis in the Kerr (2023) analysis. This profile, if isolated, would not be compact, but in a knot it is, as shown by figure 1.

There are these further differences with the Kerr (2023) trefoils. A different size, a different core circulation and it is perturbed. The size and circulation change the characteristic nonlinear timescale t_{NL} (1.10) and related times such as t_x , accordingly.

Furthermore, the perturbation changes the sequence of reconnection phase events that eventually lead to the production of the finite-time, finite energy dissipation in figure 4. The graphics in figures 10, 11, 12 and 13 for $t = 24, 30, 42$ and 48 show the preliminary steps, but do not continue into the final dissipation phase, which will require another paper. Several isosurfaces and/or views are shown for each of these times.

The major change in how this perturbed trefoil self-reconnects comes from how the vorticity structures evolve at and around the three trefoil crossings, or knots. To begin, vortex sheets are shed from only two of the knots. These sheets then interact with one another and generate the vorticity maxima around the location of the third knot. And it is within this region that the $t > 40 = t_x$ enstrophy growth accelerates as reconnection begins to split it apart.

Figure 10 presents two views of the two vortex sheets that have formed by $t = 24$. The origin of the negative helicity sheets begins with the positions of the minima (maximum

negative values) of the h_f transport term in the helicity budget equation (1.13), which Kerr (2023) studied in detail.

What the local h_f terms do is they push $h > 0$ towards local maxima of the helicity and vorticity on the vortex lines, $h < 0$ in the opposite direction and they flatten the vortex tubes due to the coincidence of the local $\min(h_f)$ with local vorticity compression. That is local negative maxima of the enstrophy production term ζ_p in (1.12).

- Now consider the maroon star at the bottom of figure 10a with one of the local negative h_f . $h > 0$ is flowing towards the local $\max(h)$, blue hexagon to the right.

- And $h < 0$ to the left, towards the global $\min(h) < 0$ at the edge of the developing $h < 0$ sheet highlighted in 10b.

- Where the global $\min(h_f)$ is located there is also local $\min(\zeta_p) < 0$ enstrophy compression (1.12), which is pushing that $h < 0$ out into the developing sheet.

These vortex sheets do not appear simultaneously due to the initial perturbation and the frames of figure 10 at $t = 24$ can tell us about the origins of that later progression. The details are:

- Figure 10a is a tilted $x - y$ plan view that indicates all three zones of activity while also highlighting the first yellowish $h \leq 0$ vortex sheet on the right. This sheet originated from the blue star near the top, the position of ω_m at $t = 21$, with its first growth shown by the orange blob to its right. At $t = 24$ this sheet is sitting between two legs of the original trefoil on the right.

- The focus of Figure 10b is upon the vortex sheet on the left in 10a from a different perspective. This sheet is being actively spawned out of the the new positions of ω_m , $\max(h) = h_{mx}$, $\min(h) = h_{mn}$ and $\min(h_f)$, the helicity flux minimum (1.13), whose importance in spawning vortex sheets has been recently discussed (Kerr 2023).

- The third location of strong activity at $t = 24$ is indicated by the maroon \star at the bottom. This location will not generate its own vortex sheet. Instead, starting at $t \sim 30$, this becomes the location around which the two previously generated sheets wrap around one another.

- Another role played by the vortex sheets as they extend over time is in how their unseen edges reach the periodic boundaries, which then push back against the growing sheets. This effect can provide us with an empirical explanation for the origin of the observed critical domain size parameter $\ell_c \sim \nu^{-1/4}$ (2.1). Another example of the expanding sheets is given by figure 22 of Kerr (2023).

Reconnection phase figures 11 and 12 at $t = 30$ and 42 show the further development around that bottom location. Both $t = 30$ frames in figure 11 have $\omega = 2$ isosurfaces. 11a is dominated by a temporally extended, smaller vorticity, $\omega = 0.25$, isosurface that is a version of the $t = 24$ helicity-mapped vortex sheets from figure 10a and is overlaid with several higher vorticity gray (single colour) isosurfaces. Two small, remnant gray surfaces at the top of 11a show where the knots that created the two $t \leq 24$ surfaces were, with a major convoluted surface at the bottom of figure 11a being where those two $t = 24$ isosurfaces are now interacting.

Figure 11b maps the helicity onto that higher vorticity isosurface at the bottom, generating a structure that shows how the already generated vortex sheets are being pulled together, then starting to wrap around one another. All the primary vorticity and helicity-related extrema are within this structure.

By $t = 42$, the outer vortex sheets from $t = 30$ have begun to dissipate, leaving behind in figure 12a a $\omega = 0.96$ local jellyroll of vortex sheets. This jellyroll might be separating from the rest of the trefoil, with the $\omega = 0.25$ isosurface in 12b showing some remaining connection to that outer structure of the trefoil. A high threshold $\omega = 31$ isosurface is

included in figure 12b to demonstrate that distinct coiled vortex structures exist within the $\omega = 0.96$ isosurfaces above.

The outer $\omega = 0.73$ isosurfaces at $t = 48$ in figure 13a show that the jellyroll separation noted at $t = 42$ can now be describing as a splitting, with the inner $\omega = 2.1$ isosurfaces in figure 13a showing spiraling vortices around the two halves of the split knot. This suggests how for each of these halves enstrophy growth can accelerate sufficiently to generate the convergent dissipation rates in figure 4, and could also be the source of the transient span of mid-wavenumber Kolmogorov scaling $Z_V(k) \sim k^{1/3}$ regimes in figure 9b. One mechanism that might explain the origin of this enstrophy increase and beginnings of Kolmogorov scaling is the spiral vortex model (Lundgren 1982). Showing how this wrapping, or an equivalent small-scale dynamics, continues to later times will be the topic of another paper.

5. Summary of using large $(2\ell\pi)^3$ domains.

This paper has focused upon two aspects of the large domain, higher Reynolds number trefoil calculations that were not fully covered by the earlier trefoil calculations of Kerr (2018b) and Kerr (2023). The first aspect, in sections 2.1 to 4, extends the numerical analysis of the perturbed trefoil calculations from before (Kerr 2018b), with later times and higher resolution for most, plus one new calculation.

These extensions begin with enlargements of the computational domains at mid- to late-times so as to maintain the observed temporal convergence of $\sqrt{\nu}Z(t)$ at $t = t_x \approx 40$ in figure 2, and then approximate convergence of the dissipation rate $\epsilon = \nu Z$ for $t \sim t_\epsilon = 93 \sim 2t_x$ in figure 4. This enlargement included the smallest viscosities/highest Reynolds numbers calculations, all of which are indicated by dot-dash lines and are somewhat under-resolved, These are $\nu = 1.56 \times 10^{-5}$, 7.8×10^{-6} , and 4×10^{-6} . Previously $t_x \approx 40$ was identified from vortex structures as the end of the reconnection phase (Kerr 2018a), and then as the transition from the inverse-linear $(\sqrt{\nu}Z(t))^{-1/2}$ behaviour (Kerr 2018b), as in figure 3, to accelerated enstrophy growth that leads to convergence of the energy dissipation rates $\epsilon = \nu Z(t)$ in figure 4. That $t_x \approx 40$ is the time when physical space reconnection begins is shown here using graphics at $t = 42$ and 48 in figures 12 and 13.

Figure 4 shows that the convergence of $\epsilon(t)$ begins at $t \sim 70$ and persists for approximately $\Delta T \sim t_x$, which is long enough that when temporally integrated yields approximately ν -invariant finite ΔE_ϵ (1.2), satisfying one definition for a *dissipation anomaly*. This $\epsilon(t) = \nu Z = \nu \mathcal{O}_{V_1}^2$ convergence can be obtained over the full factor of 125 decrease in ν and is consistent with these being turbulent flows. However, convergence of the higher-order $m > 1$ $\mathcal{O}_{V_m}(t)$ moments at these later times can only be achieved over a factor of 25 in the Reynolds number. Figure 9 shows that for these mid-range Reynolds numbers, the mid-wavenumber spectral slopes are Kolmogorov-like, providing further evidence for the appearance of classical turbulence.

5.1. Supporting numerical analysis and mathematical scaling for $(2\ell\pi)^3$ domains.

The second aspect is providing new quantitative numerical analysis and mathematical scaling to explain why the computational domains need to be increased. Because they are compact, trefoil vortex knots have been ideal for showing that the $B_\nu(t)$ (1.14) scaling can be retained as ν decreases by increasing the domain size, leading to this question: What controls the domain dependence of the enstrophy suppressing critical viscosities?

Previously, to maintain the temporal convergence at t_x , the domain size $\mathcal{L} = 2\ell\pi$ had to be empirically increased as ν decreased (Kerr 2018a,b). Although an estimate of that dependence was not given. Here, with a wider range of ν , especially for the convergence

(a)

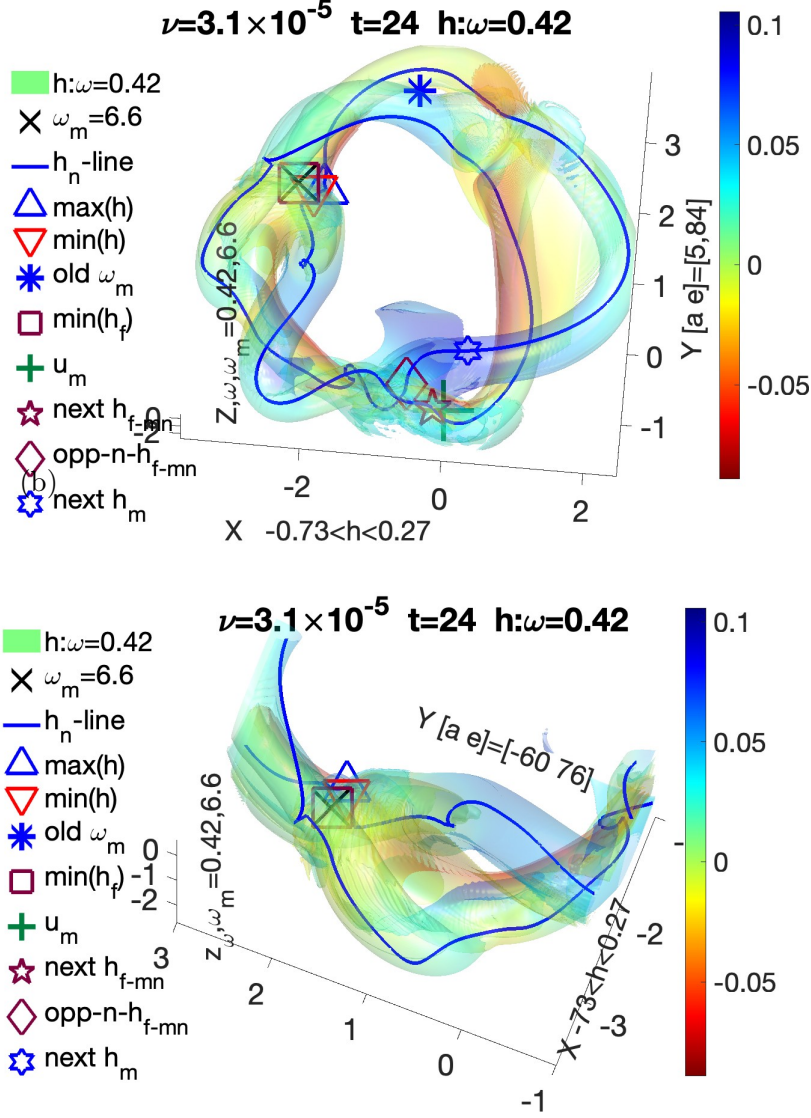


FIGURE 10. (a) Helicity-mapped vorticity isosurfaces from the $6\pi\nu = 3.125 \times 10^{-5}$ trefoil vortex knot showing the appearance of reddish to yellow negative helicity, vortex sheets. These are being shed off the blue, predominantly positive helicity of the core of the trefoil vortex. This is similar to what is shown for three-fold symmetric trefoils (Kerr 2023) at $t = 3.6t_{NL}$. This trefoil was perturbed so it is not perfectly three-fold symmetric and the evolution of the sheets at the three crossing locations are at different stages of sheet formation and development. Five primary locations are noted: $\max(\omega) = \omega_m = 6.6$, $\max(h) = h_{mx}$, $\min(h) = h_{mn}$ and $\min(h_f) = h_{f-mn}$. The formation of the yellowish $h \lesssim 0$ sheet on the right began $t \gtrsim 21$ around the $t = 21 \omega_m$ position, the blue * at the top. The sheet on the left is forming around the current $t = 24$ positions of the ω_m , $\max(h)$ and $\min(h)$ and minimum of the vortical helicity flux $\min(h_f)$, all in the upper left. A third sheet formation might have formed at the bottom, but in this asymmetric case what happens instead is that the pre-existing sheets wrap around one another, as shown in the next two figures. (b) Focus on left zone vortex sheets around the positions of ω_m , $\max(h)$ and $\min(h)$, rotated such the sheets are exposed. The strongest $h < 0$ is coming off the outer (bottom) trefoil leg, with a yellow $h \lesssim 0$ vortex sheet between the two legs of the trefoil.

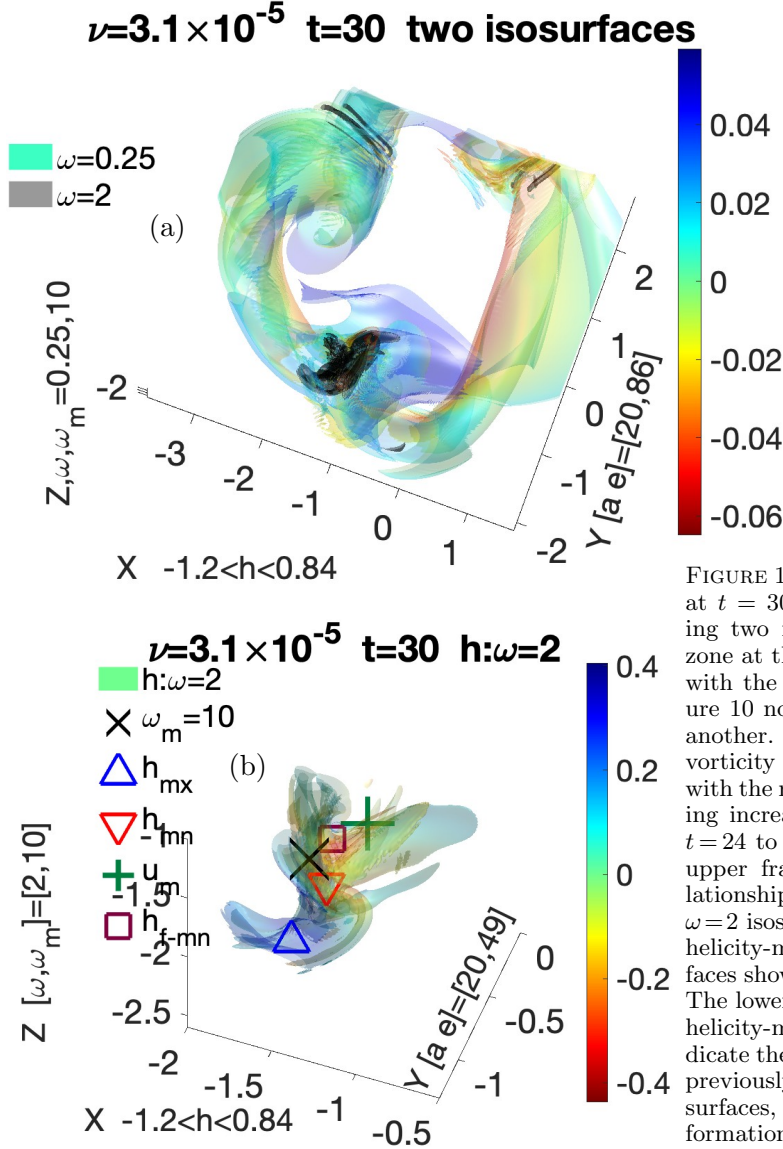


FIGURE 11. Vorticity isosurfaces at $t = 30$. This and the following two figures focus upon the zone at the bottom from $t = 24$, with the vortex sheets from figure 10 now winding around one another. In both frames, $\omega = 2$ vorticity isosurfaces are shown with the maximum vorticity having increased from $\omega_m = 6.6$ at $t = 24$ to $\omega_m = 10$ at $t = 30$. The upper frame (a) shows the relationship between the primary $\omega = 2$ isosurface in black and the helicity-mapped $\omega = 0.25$ isosurfaces show the rest of the trefoil. The lower frame (b) uses a $\omega = 2$ helicity-mapped isosurface to indicate the active wrapping of the previously ($t = 24$) formed isosurfaces, which is leading to the formation of an intense localised vortex knot.

of $(\nu^{1/4}\Omega_\infty)^{-1}$ at $t_\infty \approx 18.4$, plus the consistency of the convergence of each ($t < t_x$) $(\nu^{1/4}\mathcal{O}_{V_m}(t))^{-1}$, it is clear that the increase is $\ell \sim \nu^{-1/4}$. With the structural evidence pointing to the growth of vortex sheets as in figures 10 and 11a as the source of the limiting factor. Overall, combining the requirements at large scales with $\ell \sim \nu^{-1/4}$, with those at small scales going as $\eta \sim \nu^{3/4}$, the range of scales should increase as $\ell/\eta \sim \nu^{-1/4}/\nu^{3/4} \sim \nu^{-1}$.

A more rigorous supporting result is given in the appendices. This provides an extremal mathematical justification for why increasing ℓ is needed. The method consists of determining domain size dependent mathematical critical viscosities $\nu_s(\ell)$ as ℓ increases. These analytic/Sobolev $\nu_s(\ell)$ are found by rescaling the high-order $s > 5/2$ Sobolev analysis for $\ell = 1$, $V = (2\pi)^3$ into larger $V_\ell = (2\ell\pi)^3$ domains. With some $(2\pi)^3$ estimates

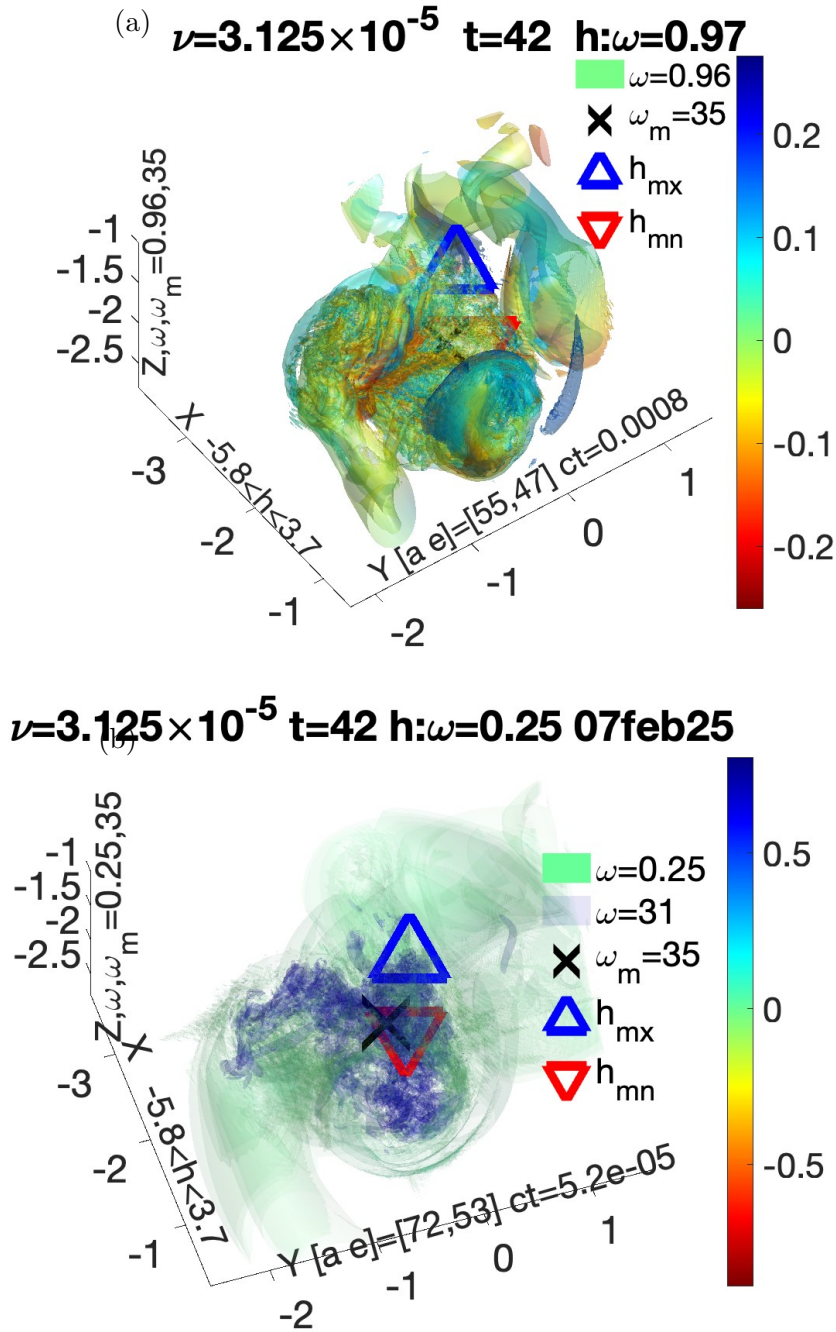


FIGURE 12. Frame (a) shows a continuation of the inner (left-side) $\omega = 1$ vorticity isosurfaces trends begun at $t = 30$ in figure 11b using a $\omega = 0.96$ isosurfaces. With the maximum vorticity increasing from $\omega_m = 10$ at $t = 30$ to $\omega_m = 35$ at $t = 42$. The more tightly wound structure on the right has within it the barely visible vorticity and helicity extrema, with the maximum vorticity increasing from $\omega_m = 10$ at $t = 30$ to $\omega_m = 35$ at $t = 42$. This increase in ω_m is a prelude to the accelerated enstrophy production for $t > t_x \sim 40$. A new feature is a series of vortex tubes on the left that have aligned with one another. Frame (b) shows two additional isosurfaces with the positions of h_{\max} , h_{\min} and ω_m shown. The helicity-mapped $\omega = 0.25$ isosurface shows how this knot is connected to the rest of trefoil and the $\omega = 31$ isosurface shows the coiled vortex structure within the wound up structure shown above.

tr6piQ4nu312 t=48 30jan25 h: $\omega=0.73$

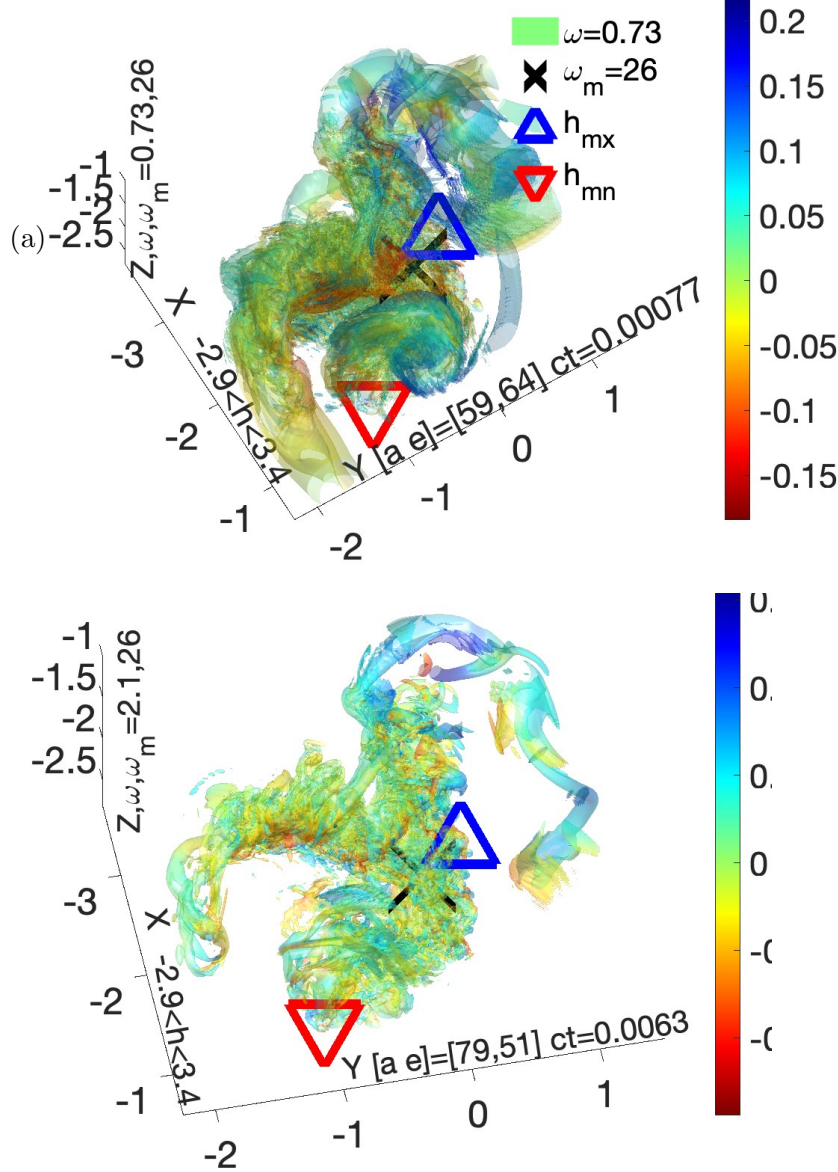


FIGURE 13. The $\omega = 0.73$ isosurface in (a) is similar to that from $t = 42$, except there is a clearer separation between the left side and wound-up right side. The $\omega = 2.1$ isosurface in (b) makes this post- $t = 42$ split more obvious with spirals wrapping around their respective centrelines. The dynamics of these spirals as it continues would be consistent with the accelerated growth in the enstrophy that leads to the finite dissipation ΔE_ϵ shown in figure 4.

of the ν_s made from the Euler norms in appendix A.5, before they are transformed into the original domain in appendix A.6.

Is there mathematics that could bring the two determinations of the critical viscosities more in line with one another? Currently we know that the $\nu_s(\ell)$ should be, and are, orders of magnitude smaller than the empirical ν_c . However, it is believed by many that

$\ell \rightarrow \infty$ limiting behavior can be determined by a more direct extension of the $(2\pi)^3$ mathematics (Constantin 1986) to whole space, infinite \mathbb{R}^3 . Having such an extension written down explicitly might be helpful in determining $\nu_s(\ell)$ and bridging that gap.

The conclusion of both approaches is that getting a *dissipation anomaly*, that is finite-time finite ΔE_ϵ , without finite-time singularities is possible only when the physical problem is done in whole space, that is infinite \mathbb{R}^3 .

5.2. Does $(2\ell\pi)^3$ rescaling lead to turbulence?

Does evidence for a *dissipation anomaly* and Kolmogorov spectra imply that turbulent scaling is obeyed? For example, by following the seminal ideas of Onsager (1949), one explanation for the origins of finite dissipation, structure function scaling and how $k^{-5/3}$ Kolmogorov spectra form is to assume the existence of singularities with the velocity increments in space having a 1/3 Hölder exponent (Eyink 2003).

However, the latest forced, very high Reynolds numbers calculations are not providing convincing numerical evidence because the dissipation rate ϵ (1.11) increases slowly when the Reynolds numbers are increased (Iyer *et al.* 2022). Given these difficulties, the primary evidence in favor of the existence of finite ΔE_ϵ in turbulent flows is still largely experimental (Vassilicos 2015; Schmitt *et al.* 2024).

Due to these limitations upon the Navier-Stokes direct numerical simulations, alternative explanations for how finite-time dissipation can form have been proposed. These include whether there are recurrent quasi-singular events, or whether additional sub-Kolmogorov fluctuations have roles (Eyink & Jafari 2022). Or maybe boundary layer singularities (Lou & Hou 2014) might trigger significant interior three-dimensional dissipation rates. None of these possibilities has been demonstrated using three-dimensional simulations that have been run over a range of viscosities.

The references just given take the point of view that scaling of structure functions are critical. Eventually an attempt to find structure functions for a compact numerical data set should be done. Most likely following a method similar to what has been applied to steady-state, homogeneous flows (Kerr *et al.* 2001). However, like the spectral scaling in section 3, those results would be time-dependent and less conclusive than desired.

The calculations here present an alternative approach to generating numerical turbulence where the large-scale forcing is replaced by large-scales that grow without bounds. Demonstrating that the incompressible Navier-Stokes, without the types of corrections suggested above, are capable of generating finite-time energy dissipation and signs of Kolmogorov scaling, which is one manifestation of Onsager's 1/3 scaling.

6. Summary

To close this paper, a number of questions are now presented, some of which are currently being addressed.

Is convergent scaling by $\sqrt{\nu}Z(t) = (\nu^{1/4}\mathcal{O}_{V_1}(t))^2$, unique to trefoils? In published calculations the equivalent $B_\nu(t) = (\nu^{1/4}\mathcal{O}_{V_1})^{-1}$ scaling (1.14) has been identified for trefoils with different core thicknesses (Kerr 2018a), symmetric trefoils in a $(2\pi)^3$ periodic box (Kerr 2023), and nested coiled rings (Kerr 2018c). And in ongoing work, $\mathcal{O}_{V_m}(t)$ scaling (1.1) is being applied to the Taylor-Green vortex (Brachet *et al.* 1983) and new versions of recent orthogonal vortices calculations (Ostillo-Monico *et al.* 2021).

What is the origin of the $\nu^{1/4}$ scaling? Lengths with a $\sqrt{\nu t}$ dependence are common in fluid theory. One example is how the compression perpendicular the stretching along Burgers vortex is balanced by the perpendicular viscous terms. Another example is how some of the most refined mathematics uses Leray (1934) scaling with $\delta_\nu(t) \sim \sqrt{2\nu(T-t)}$

to restrict singularities of the Navier-Stokes equations (Necas *et al.* 1996; Escauriaza *et al.* 2003). However Leray scaling is about collapse to a point, not to type of sheets observed here.

Could these vortex sheets be the source of the $\nu^{1/4}$ scaling? An answer comes from how the sheets form out of the helical knots within the trefoil configurations, here and in (Kerr 2023), which are themselves strongly helical. These knots exist where the loops of the trefoil cross and tend to block the evolution of the trefoil. However, by forming negative helicity vortex sheets like those in figures 10 and 11, a mechanism exists for circumventing those helical patches. For example, the formation of $h < 0$ vortex sheets is balanced by simultaneous increases of $h > 0$ on the trefoil's cores in Kerr (2023), allowing for increases in the vorticity along those cores without violating the pre-reconnection, nearly Euler, conservation of helicity.

The new work with initial orthogonal vortices shows that each vortex contributes its own sheet, to create a pair. With the compression pushing the vortices together again being balanced by viscous diffusion. This results in the inverse slope (a length) on the boundaries of each sheet going as $\delta(\nu) \sim \nu^{1/2}$, balanced by expansion and stretching in the two perpendicular directions that goes as $\nu^{-1/4}$.

Does the influence of $\nu^{1/4}$ scaling and formation of double vortex sheets extend further in time? It does in the sense that double vortex sheets are required for the post-reconnection enstrophy growth to accelerate sufficiently to get finite-time energy dissipation, ΔE_ϵ (1.2) and is consistent with how the wrapped structure at the bottom of figure 11 at $t = 30$ has formed from the two vortex sheets at $t = 24$ in figure 10. The spiral vortex model of Lundgren (1982) assumed only a single vortex sheet spiraling around a central vortex, which is distinctly different than the paired sheets of both this trefoil and orthogonal vortices.

To accomplish any of these further objectives, new calculations will be required. Starting with extending the Reynolds number range of the $m > 1$ $\Omega_m(t)$ convergence in figures 6 to the $\nu = 1.56 \times 10^{-5}$ and $\nu = 7.8 \times 10^{-6}$ cases, which should be re-run in $(8\pi)^3$ domains on 4096^3 , or equivalent, meshes. This should provide for both adequate resolution on the small scales and sufficient padding on the large scale to control interactions with the periodic boundaries.

Acknowledgements

I would like to thank the Isaac Newton Institute for Mathematical Sciences for support and hospitality during the programme *Mathematical Aspects of Fluid Turbulence: where do we stand?* in 2022, when work on this paper was undertaken and supported by grant number EP/R014604/1. Further thanks to E. Titi (Cambridge) who suggested using domain rescaling and J.C. Robinson (Warwick) who shared his version of the earlier nonlinear inequality (Constantin 1986).

Appendix A. Domain rescaling

Can the empirical evidence for dependence of $\nu_c(\ell)$ (2.1) be understood analytically? These appendices show that how related analytic critical viscosities ν_s , originally estimated using $(2\pi)^3$ analysis (Constantin 1986), decrease as ℓ increases through rescaling of that analysis to larger $(2\ell\pi)^3$, $\ell > 1$, domains. Which in turn allows the formation of *dissipation anomalies* as ℓ increases.

In the past it has been claimed that this can be done by supposing extensions into whole space, infinite \mathbb{R}^3 , using the “usual methods”. One version of that approach is to create new outer, whole space length scales out of ratios of higher-order Sobolev norms. An approach that requires additional estimates that might also depend upon the viscosity.

The approach here is incremental, showing how the $\nu_c(\ell)$ change as ℓ increases. The description will be more physically-based than mathematically-based as in Robinson (2021).

Appendices A.2-A.6 show how one can apply scale invariance to avoid introducing new length scales when extending that analysis to larger $V_\ell = (2\ell\pi)^3$ domains. First, one rescales the V_ℓ inner products and norms into a $(2\pi)^3$ domain; then one can calculate the critical viscosities $\nu_{s_{2\pi}}$ as before; and finish by converting the $\nu_{s_{2\pi}}$ into ν_s in the original V_ℓ domain. The primary tools for this analysis are the $\dot{H}_\ell^s = \|u_\ell\|_s^2$ norms (1.19) defined in section 1.2.

Before the rescalings are given, appendix A.1 presents the domain dependent rescaling of the variables, properties and norms that will be used throughout. The first rescaling step in appendix A.2 then applies those rescalings to squeezing the $\|u_\ell\|_{\dot{s}+1}$ the Navier-Stokes solutions in large $V_\ell = (2\ell\pi)^3$ domains into a $(2\pi)^3$ domain, followed by application of the resulting $\|u_\lambda\|_{\dot{s}+1}$ ($\lambda = \ell$) to approximations of the $H_{2\pi}^s$ Sobolev mathematics developed for $(2\pi)^3$ domains.

Next, appendix A.3 determines difference inequalities for the $w = v - u$ equations (1.6), with appendix A.4 providing an alternative way to solve the cubic nonlinearity in those inequalities with integrating factors. This is followed by the determination of the critical viscosities $\nu_{s_{2\pi}}$ in appendix A.5 using the $H^{s_{2\pi}}$ norms. The sequence of steps in appendices A.3 to A.5 follows Chapter 9 of Robinson *et al.* (2016) and is analogous to what was previously found for a $(2\pi)^3$ domain (Constantin 1986).

Finally, those $\nu_{s_{2\pi}}$ are rescaled back to the original $(2\ell\pi)^3$ domain in appendix A.6, resulting in decreasing $\nu_s \sim \exp\left(-\int_0^t \lambda^{s+1} \|u_\ell(\tau)\|_{\dot{s}+1} d\tau\right) \lambda^3$ as $\lambda = \ell$ increases, with the $\|u_\ell(\tau)\|_{\dot{s}+1}$ coming from the original domain and the exponential factor dominating over the algebraic λ^3 factor.

This result can explain why the small ν trefoil results with convergent $\sqrt{\nu}Z(t)$, and then convergent $\epsilon = \nu Z(t)$, are allowed by the mathematics. And if extended further by taking $\ell \rightarrow \infty$, one might be able identify limiting behaviour in \mathbb{R}^3 , known as whole space.

A.1. Rescaling of variables and norms.

For a periodic domain of size $V_\ell = (2\ell\pi)^3 = L^3$, $L = 2\pi\ell$, a rescaling parameter $\lambda = \ell$ is defined that rescales these variables into a $L_0 = 2\pi$, $L_0^3 = (2\pi)^3$ domain:

$$L_\lambda = L/\lambda = 2\pi, \quad U_\lambda = U/\lambda, \quad u_\lambda = u/\lambda \quad \text{and} \quad \nu_\lambda = \nu/\lambda^2 \quad (\text{A } 1)$$

such that the Reynolds numbers and inverse time/vorticity scales invariant under λ :

$$Re_\lambda = U_\lambda L_\lambda / \nu_\lambda = Re, \quad \omega_\lambda = \nabla_\lambda \times u_\lambda = (\lambda/\lambda)\omega = \omega. \quad (\text{A } 2)$$

The inverse lengths and derivatives when mapped into a L_λ domain are multiplied by λ (left), with their effect upon u (right) as follows:

$$\partial_\lambda = \lambda \partial, \quad \nabla_\lambda = \lambda \nabla, \quad \nabla^s u \rightarrow \nabla_\lambda^s u_\lambda = \lambda^{s-1} \nabla^s u = \lambda^{s-1} u_{,s} \quad (\text{A } 3)$$

such that for $\|u\|_s$ in the V_ℓ domain (left), in the V_1 (right) domain one gets

$$\|u_{,s}\|_0 = \|u\|_s = \left(\int_{V_\ell} (\nabla^s u)^2 d^3x \right)^{1/2} \Rightarrow \|u_\lambda\|_s = \left(\int_{V_1} \lambda^{2s-2} (\nabla^s u_\lambda)^2 d^3x \right)^{1/2} = \lambda^{s-1} \|u\|_s \quad (\text{A } 4)$$

A.2. Squeezing, then rescaling, H^s norms

Now extend this scaling to vorticity-related properties and Sobolev norms.

a) For the circulation:

$$\Gamma_\lambda \sim U_\lambda L_\lambda = \Gamma / \lambda^2 \quad \text{and} \quad a_\lambda = a / \lambda, \quad (\text{A } 5)$$

b) The nonlinear timescale is invariant:

$$T_{NL} = T_\lambda = a_\lambda^2 / \Gamma_\lambda = (a^2 / \lambda^2) / (\Gamma / \lambda^2) = T_{NL}. \quad (\text{A } 6)$$

c) The volume-integrated enstrophy $Z = V \|u\|_1^2 \sim \Gamma^2 / L$ such that

$$Z_\lambda \sim (\Gamma^2 / L) = Z / \lambda^3 \quad (\text{A } 7)$$

d) The volume-integrated energy $E = \frac{1}{2} V \|u\|_0^2 \sim \Gamma^2 L$ so that

$$E_\lambda \sim \Gamma^2 L / (\lambda^2 \lambda^2 \lambda) = E / \lambda^5 \quad (\text{A } 8)$$

e) Finally, the viscous timescale is unchanged:

$$t_\nu = \nu_\lambda \Delta_\lambda u / u \sim \nu / \lambda^2 (\lambda^2 \Delta u / \lambda) / (u / \lambda) \sim \nu \Delta u \quad (\text{A } 9)$$

Classical result Does this rescaling affect the Hölder and Cauchy-Schwarz inequalities that lead to this time inequality Doering (2009)? (see also Robinson (2021))

$$\frac{d}{dt} \|\nabla u\|_0^2 \leq \frac{c'}{\nu^3} \|\nabla u\|_0^6. \quad (\text{A } 10)$$

c' is constant that is independent of the periodic domain size. From this one gets for $u_0 = u(0)$

$$\|\nabla u(\cdot, t)\|_0^2 \leq \frac{\|\nabla u_0\|^2}{\sqrt{1 - 2c' \|\nabla u_0\|^4 t / \nu^3}} \quad (\text{A } 11)$$

Using the denominator of this inequality, the times over which the solutions are ensured to be smooth and unique are

$$0 < t < t_b = \frac{\nu^3}{2c' \|\nabla u_0\|^4} \quad (\text{A } 12)$$

Because the rescaled viscosity is $\nu_\lambda^3 = \nu / \lambda^6$ and enstrophy squared is $Z_\lambda^2 = \|\nabla u\|^4 \sim Z / \lambda^6$, after rescaling $t_{b\lambda} = t_b$. Such that this time scale (A 9) is not affected by the rescaling with λ .

A.3. Difference inequalities for w with Euler u .

For $\ell = 1$, by using higher- s -order Sobolev time nonlinear inequalities one can find the $(2\pi)^3$ domain, analytic critical viscosities ν_s that mark the threshold for when $\nu \rightarrow 0$ Navier-Stokes solutions can be bounded by $\nu \equiv 0$ Euler solutions. Higher- s -order Sobolev

time nonlinear inequalities are used because they allow us to go beyond what the $s = 0$ $(d/dt)^{\frac{1}{2}}\|u\|_0^2$ equation (1.17) can tell us. The method used is an alternative to Constantin (1986) outlined by Robinson *et al.* (2016). †

The relevant Sobolev time inequalities are higher-order versions of the s -order inner products between the velocity difference $\mathbf{w} = \mathbf{v} - \mathbf{u}$, higher-order time derivatives $\nabla^s w_t$ and its equation (1.6).

$$\frac{1}{2} \frac{d}{dt} \|w\|_s^2 + \nu \|w\|_{s+1}^2 \leq \nu \|u\|_{s+1} \|w\|_{s+1} + d_s \|w\|_s^3 + d_s \|u\|_s \|w\|_s^2 + c_s \|u\|_{s+1} \|w\|_s^2 \quad (\text{A } 13)$$

The resulting inequality equations have several cubic nonlinearities and two sets of constants. For order s terms, c_s , and for nonlinear order $s + 1$ terms, d_s .

$$c_s = 2^s C_s \quad \text{and} \quad d_s = s 2^s C_{s-1} \quad \text{with} \quad C_s \sim L^{-3/2+s}. \quad (\text{A } 14)$$

The goal is to reduce (A 13) to an inequality with a single cubic nonlinearity. Then solve it to show if there are bounds upon Navier-Stokes solutions.

To get (A 13), gradients need to be added to the $B_{NL}(\cdot, \cdot)$ inner products in the w equation (1.6). These become order- s inner products $\langle uv \rangle_s^2$ (1.16), from which w -based energy inequalities can be created. For example

$$\|B_{NL}(u, w)\|_s \leq c_s \|u\|_s \|w\|_{s+1}. \quad (\text{A } 15)$$

To find the analytic ν_s , some reductions are needed. The next step is make estimates of the higher- s , inner products of higher-order versions of the three $B_{NL}(\cdot, \cdot)$ nonlinear terms of the \mathbf{w} equation (1.6): $(\mathbf{u} \cdot \nabla) \mathbf{w}$, $(\mathbf{w} \cdot \nabla) \mathbf{u}$, $(\mathbf{w} \cdot \nabla) \mathbf{w}$ after contraction with $\hat{\mathbf{w}}_{\mathbf{k}}$ as in (1.17). This contraction converts these quadratic nonlinearities into cubic nonlinearities.

To reduce the multiple cubic terms into a single cubic nonlinearity requires either raising or lowering the order of the components terms, a process that through the c_s and d_s (A 14) effectively introduces a length scale of 2π into the nonlinear inequality analysis. If the s -order can be retained then c_s is used and only $s > 3/2$ analysis is required. Starting with how this two s -order inner products is absorbed between a test function \mathbf{w} and $B_{NL}(\cdot, \cdot)$.

$$|(B_{NL}(w, u), w)_s| \leq c_s \|u\|_{s+1} \|w\|_s^2. \quad (\text{A } 16)$$

However, to handle the nonlinear time inequality needed to find the ν_s in H_s , d_s and $s \geq 5/2$ is required. A rigorous argument from Constantin & Foias (1988) shows how order reduction of the inequality analysis can be done when higher-order $s > 5/2$ is used. Specifically the order $s + 1$ terms can be reduced to order s by using the constant d_s (A 14), so that the $\|\cdot\|_{s+1}$ terms in (A 16) are converted into following $\|\cdot\|_s$.

$$|(B_{NL}(w, w), w)_{H^s}| \leq d_s \|w\|_s^3 \quad \text{and} \quad |(B_{NL}(u, w), w)_{H^s}| \leq d_s \|u\|_s \|w\|_s^2. \quad (\text{A } 17)$$

The first term converts the $B_{NL}(w, w)$ term into $\|w\|_s^3$, a cubic nonlinearity, and the second allows the $B_{NL}(u, w)$ term to be paired with $B_{NL}(w, u)$ term to form an integrating factor.

The next steps reduce the two viscous terms into a single term on the right-hand side using Young's inequality $ab \leq \frac{1}{2} \left(\epsilon a^2 + \frac{b^2}{\epsilon} \right)$ with $\epsilon = 1/2$ to combine the first term on the right with the $\nu \|w\|_{s+1}^2$ on the left. Then the last two terms are combined by using

† The approach in A.5 and A.6 closely follows Chapter 9 of (Robinson *et al.* 2016), with Lemma 1 of the robustness proof being a version by the solution to problem 9.2.

Cauchy-Schwarz upon the left one, that is $d_s \|u\|_{\dot{s}} \leq Lc_s \|u\|_{\dot{s}+1}$ to get

$$\frac{1}{2} \underbrace{\frac{d}{dt} \|w\|_{\dot{s}}^2}_{L^{5-2s}T^{-3}} \leq \underbrace{\frac{\nu}{4} \|u\|_{\dot{s}+1}^2}_{(L^2T^{-1})(L^{3-2s}T^{-2})} + \underbrace{d_s \|w\|_{\dot{s}}^3}_{(L^{-5/2+s})(L^{15/2}T^{-3})L^{-3s}} + \underbrace{2c_s}_{M_s \sim L^{-3/2+s}} \underbrace{\|u\|_{\dot{s}+1} \|w\|_{\dot{s}}^2}_{(L^{15/2}T^{-3})L^{-3s-1}}. \quad (\text{A } 18)$$

Underbraces are included to demonstrate the consistent order of each of its terms after the conversion of the $\|\cdot\|_{\dot{s}+1}$ (A 16) into $\|\cdot\|_{\dot{s}}$ in (A 17). †

A.4. Solving the difference inequalities for w with Euler u .

The last term on the right in (A 18) can be used to create these integrating factors:

$$E_s(t) = \exp\left(\int_0^t M_s \|u(\tau)\|_{\dot{s}+1} d\tau\right), \quad M_s = d_s L + c_s = s2^s C_{s-1} L + 2^s C_s, \quad (\text{A } 19)$$

which with $C_s = L^{-3/2+s}$ becomes $M_s \sim s2^s L^{-3/2+s}$. This allows (A 18) to be rewritten as

$$\frac{d}{dt} (E_s^{-2}(t) \|w(t)\|_{\dot{s}}^2) \leq \frac{\nu}{2} \|u\|_{\dot{s}+1}^2 E_s^{-2}(t) + 2d_s E_s(t) \|w\|_{\dot{s}}^3 E_s^{-3}(t). \quad (\text{A } 20)$$

Then by defining

$$X(t) = E_s^{-2}(t) \|w(t)\|_{\dot{s}}^2, \quad \alpha(t) = 2d_s E_s(t) \quad \text{and} \quad f(t) = \|u\|_{\dot{s}+1}^2 E_s^{-2}(t), \quad (\text{A } 21)$$

and using the following Lemma, including the restrictions of (A 23, A 25, A 26), one obtains an improved bound using $X(t)$.

Lemma 1. *Suppose that $X \geq 0$ is continuous and*

$$\dot{X} \leq \alpha(t) X^{3/2} + (\nu/2) f(t), \quad X(0) = 0, \quad (\text{A } 22)$$

for some $\alpha(\cdot) > 0$ and f positive and integrable on $[0, T]$. Then for $X(t) < \infty$ assume

$$\nu \left(\int_0^t \alpha(s) ds \right) \left(\int_0^t f(s) ds \right)^{1/2} < 1; \quad (\text{A } 23)$$

and by applying rules for integration by parts to the right-hand-side of (A 22) one gets

$$X(t) \leq \frac{(\nu/2) \int_0^t f(\tau) d\tau}{\left[1 - (2\nu)^{1/2} \left(\int_0^t \alpha(\tau) d\tau \right) \left(\int_0^t f(\tau) d\tau \right)^{1/2} \right]^2}, \quad (\text{A } 24)$$

while

$$8\nu \left(\int_0^t \alpha(s) ds \right)^2 \left(\int_0^t f(s) ds \right) \leq 1; \quad (\text{A } 25)$$

and this bound holds:

$$X \leq 2\nu \int_0^t f(s) ds. \quad (\text{A } 26)$$

Proof: Start with this overestimate: On the time interval $[0, T]$ the solutions $X(t)$ of (A 22) are bounded above by the solution of

$$\dot{Y} = \alpha(t) Y^{3/2}, \quad Y(0) = (\nu/2) \int_0^T f(s) ds \quad (\text{A } 27)$$

† From a non-rigorous perspective this effectively adds an inverse length that comes from the dependence of C_s (A 14) upon L^{-1} .

Now simply observe that the solution $Y(t)$ of (A 27) satisfies

$$\frac{1}{Y(0)^{1/2}} - \frac{1}{Y(t)^{1/2}} = 2 \int_0^t \alpha(s) ds,$$

and hence

$$Y(t) \leq \frac{Y(0)}{\left[1 - \int_0^t \alpha(s) ds \left(2Y(0)^{1/2}\right)\right]^2}. \quad (\text{A } 28)$$

Finally, by defining $Y(0)$ using (A 27) one gets (A 24). \square

A.5. Using the difference inequality solutions

By re-inserting the definitions for $\alpha(t)$ and $f(t)$ (A 21) into their time integrals (A 25), one arrives at these conditions for critical viscosities ν_s : \dagger

$$8\nu_s \left(\int_0^t 2d_s E_s(\tau) d\tau \right)^2 \int_0^t \|u(\tau)\|_{\dot{s}+1}^2 E_s^{-2}(\tau) d\tau = 1, \quad (\text{A } 29)$$

such that all $\nu \leq \nu_s$ Navier-Stokes solutions are bounded by the Euler (u) solution when

$$\nu \leq \nu_s(t) = \frac{1}{8} \frac{1}{\underbrace{\left(\int_0^t 2d_s E_s(\tau) d\tau \right)^2}_{L^{-5+2s}T^2} \underbrace{\int_0^t \|u(\tau)\|_{\dot{s}+1}^2 E_s^{-2}(\tau) d\tau}_{L^{3-2s}T^{-1}}}, \quad (\text{A } 30)$$

with the dimensions in the underbraces. When multiplied, these terms have the dimension of an inverse viscosity. Note that for any ν , at very early times when $\|w(t)\|_{\dot{s}} = \|v - u\|_{\dot{s}}$ and the $X(t)$ are small, these relations are irrelevant.

When critical viscosities ν_s equivalent to (A 30) were first derived (Constantin 1986), the goal was to demonstrate the existence of this bound. Given our current understanding of the underlying Euler norms, can (A 30) be used to estimate the ν_s in terms of time integrals of $\alpha(t)$ and $f(t)$?

A first step is to replace the time integrals with approximations at the ends of their respective time spans, with the $f(t)$ integral using $E_s^{-2}(t)$ focusing upon small times and the integral with $E_s(t)$ focusing upon $d\tau \sim t$.

- For the integral with E_s^{-2} , note that $E_s^{-2}(t=0) = 1$, so for $t \sim 0$ one gets

$$E_s^{-2}(t) = \exp\left(-2 \int_0^t M_s \|u(\tau)\|_{\dot{s}+1} d\tau\right) \sim \mathcal{O}(1)$$

and can take $\Delta\tau \sim (2M_s \|u_0\|_{\dot{s}+1})^{-1}$ as $E_s^{-2}(t)$ becomes exponentially small at large t .

- For $t \sim 0$, and by taking $f(t)$ from (A 21), one gets

$$\int f(\tau) d\tau \approx \int_0^t \|u(\tau)\|_{\dot{s}+1}^2 E_s^{-2}(\tau) d\tau \sim \|u(0)\|_{\dot{s}+1}^2 / (2M_s \|u_0\|_{\dot{s}+1}) = \|u(0)\|_{\dot{s}+1} / (2M_s). \quad (\text{A } 31)$$

- For large t in $\alpha(t)$ (A 21) and assuming that for the time span in question the $\|u(\tau)\|_{\dot{s}+1}$ is very large, the focus is upon $\tau \sim t$, with the largest contributions to

$$E_s(t) = \exp\left(\int_0^t M_s \|u(\tau)\|_{\dot{s}+1} d\tau\right) \quad \text{coming over the last} \quad \Delta\tau \sim (M_s \|u(t)\|_{\dot{s}+1})^{-1}.$$

\dagger This determination of the ν_s , and the discussion in A.5 and A.6, follow earlier discussions with J. C. Robinson.

- And for $d\tau \sim \Delta\tau$, this results in

$$\int_0^t \alpha(\tau) d\tau = \int_0^t 2d_s E_s(\tau) d\tau \sim 2d_s E_s(t) / (M_s \|u(t)\|_{\dot{s}+1}). \quad (\text{A } 32)$$

Putting (A 31) and (A 32) together in (A 30), that is determining $(8(\int_0^t \alpha(t) dt)^2 (\int_0^t f(t) dt)^{-1})$, the resulting $(2\pi)^3$ domain, s -order $\nu_{s2\pi}$ bounds for ν are given by:

$$\nu \leq \nu_{s2\pi}(t) \sim \left[8 \left(2d_s E_s(t) (M_s \|u(t)\|_{\dot{s}+1})^{-1} \right)^2 (\|u(0)\|_{\dot{s}+1}) (2M_s) \right]^{-1} \quad (\text{A } 33)$$

Combining the terms, gives this estimate

$$\nu_{s2\pi}(t) \lesssim \frac{M_s^3 \|u(t)\|_{\dot{s}+1}^2}{16d_s^2 \|u(0)\|_{\dot{s}+1}} \quad (\text{A } 34)$$

Finally, for $\nu \leq \nu_{s2\pi}$ the $\|w(t)\|_s^2$ differences between the Navier-Stokes and Euler solutions are governed by:

$$\|w(t)\|_s^2 \leq 2\nu \int_0^t \|u(r)\|_{\dot{s}+1}^2 \exp \left\{ 2 \int_r^t M_s \|u(\tau)\|_{\dot{s}+1} d\tau \right\} dr. \quad (\text{A } 35)$$

Meaning that the $\nu \leq \nu_{s2\pi}$ Navier-Stokes solutions are bounded by these integrals of the Euler solutions. So unless those Euler solutions have finite-time singularities, and Meng & Yang (2024) suggests they do not, those Euler integrals will always be bounded, which in turn bounds the $\nu \leq \nu_{s2\pi}$ Navier-Stokes solutions and in particular the dissipation rate $\nu Z(t) \rightarrow 0$.

∴ Showing that Navier-Stokes solutions in $(2\pi)^3$ domains cannot develop finite energy dissipation in a finite time (1.2) as $\nu \rightarrow 0$.

The next appendix extends this result to arbitrarily large $(2\ell\pi)^3$ domains, with the $\nu_s \rightarrow 0$ as ℓ grows. Which would allow a dissipation anomaly (1.2).

A.6. Release squeezing

To estimate the ν_s critical viscosities for a compact initial condition in larger domains $(2\ell\pi)^3$, the first step is to squeeze that compact state by $\lambda = \ell$ into a $(2\pi)^3$ domain. This also means rescaling the velocities and derivatives as in (A 1) and the higher- s norms as in (A 4) giving

- $\|u_\lambda(\tau)\|_{s+1} = \lambda^s \|u_\ell(\tau)\|_{s+1}$ (A 3) for both $\tau = 0$ and $\tau = t$.
- Next, create $(2\pi)^3$ integrating factors $E_{s,\lambda}(t)$ by putting the $\|u_\lambda(t)\|_{s+1}$ in E_s (A 19).

Note that because this operation is in a $L_0^3 = (2\pi)^3$ domain, the M_s terms in $E_{s,\lambda}(t)$ do not need to be rescaled.

- Then apply $\|u_\lambda\|_{s+1}$ and $E_{s,\lambda}$ to (A 33) to get $\nu_{s2\pi}$.
- And use the inverse of $\nu_\lambda = \nu/\lambda^2$ (A 1), with $\nu_\lambda = \nu_{s2\pi}$ and $\nu = \nu_s$: giving $\nu_s = \lambda^2 \nu_{s2\pi}$.
- Leading to the following ν_s in the original domain.

$$\nu_s(t) \sim \exp \left(- \int_0^t \lambda^{s+1} \|u_\ell(\tau)\|_{\dot{s}+1} d\tau \right) \lambda^3 \frac{M_s^3 \|u_\ell(t)\|_{\dot{s}+1}^2}{16d_s^2 \|u_\ell(0)\|_{\dot{s}+1}} \quad (\text{A } 36)$$

with the exponentially-decreasing factor dominating over the algebraic λ^3 term. This decrease of the ν_s as ℓ increases is more than fast enough to support the relevance of the variable domain calculations in figure 2.

REFERENCES

- Brachet, M.E., Meiron, D.I., Orszag, S. A., Nickel, B. G., Morf, R.H., & Frisch, U. 1983 Small-scale structure of the Taylor-Green vortex. *J. Fluid Mech.* **130**, 411–452.
- Constantin, P. 1986 Note on Loss of Regularity for Solutions of the 3—D Incompressible Euler and Related Equations. *Commun. Math. Phys.* **104**, 311–326.
- Constantin, P., & Foias, C. 1988 *University of Chicago Press*. Navier-Stokes equations.
- Doering, C.R., & 2009, Annu. Rev. Fluid Mech. **41** **109**, –128 The 3D Navier-Stokes Problem.
- Donzis, D., Gibbon, J.D., Gupta, A., Kerr, R. M., Pandit, R., & Vincenzi, D. 2013 Vorticity moments in four numerical simulations of the 3D Navier-Stokes equations. *J. Fluid Mech.* **732**, 316331.
- Escauriaza, L., Seregin, G., & Sverák, V. 2003 $L_{3,\infty}$ -solutions to the Navier-Stokes equations and backward uniqueness. *Russian Math. Surveys* **58**, 211–250. translation from Uspekhi Mat. Nauk, 58 (2003), 3–44 (Russian);
- Eyink, G.L. 2003 Local 4/5-law and energy dissipation anomaly in turbulence.. *Nonlinearity* **17**, 137–145.
- Eyink, G., & Jafari, A. 2022 High Schmidt-number turbulent advection and giant concentration fluctuations. *Phys. Rev. Research* **4**, 023246.
- Gallay, T., & Smets, D. 2020 Spectral stability of inviscid columnar vortices,. *Anal. PDE* **13**, 17771832.
- Howard, L.N., & Gupta, A.S. 1961 On the hydrodynamic and hydromagnetic stability of swirling flows,. *J. Fluid Mech.* **14**, 463–476.
- Ishihara, T., Gotoh, T., & Kaneda, Y. 2009 Study of High-Reynolds Number Isotropic Turbulence by Direct Numerical Simulation. *Ann. Rev. Fluid Mech.* **41**, 165–180.
- Iyer, K.P., Sreenivasan, K.R., & Yeung, P.K. 2022 Nonlinear amplification of hydrodynamic turbulence. *J. Fluid Mech.* **930**, R2.
- Kerr, R.M. 1985 Higher-order derivative correlations and the alignment of small-scale structures in isotropic numerical turbulence.. *J. Fluid Mech.* **153**, 31.
- Kerr, R.M. 1990 Velocity, scalar and transfer spectra in numerical turbulence.. *J. Fluid Mech.* **211**, 309.
- Kerr, R.M. 2013a Swirling, turbulent vortex rings formed from a chain reaction of reconnection events. *Phys. Fluids* **25**, 065101.
- Kerr, R.M. 2013b Bounds for Euler from vorticity moments and line divergence.. *J. Fluid Mech.* **729**, R2.
- Kerr, R.M. 2018a Trefoil knot timescales for reconnection and helicity. *Fluid Dynamics Res.* **50**, 011422.
- Kerr, R.M. 2018b Enstrophy and circulation scaling for Navier-Stokes reconnection. *J. Fluid Mech.* **839**, R2.
- Kerr, R.M. 2018c Topology of interacting coiled vortex rings. *J. Fluid Mech.* **854**, R2.
- Kerr, R.M. 2023 Sensitivity of trefoil vortex knot reconnection to the initial vorticity profile. *Phys. Rev Fluids* **8**, 074701.
- Kerr, R.M., Meneguzzi, M., & Gotoh, T. 2001 An inertial range crossover in structure functions.. *Phys. Fluids* **13**, 1985–1994.
- Leray, J. 1934 Sur le mouvement d’un liquide visqueux emplissant l’espace.. *Acta Math.* **63**, 193–248.
- Hou, T.Y., & Luo, G. 2014 Potentially singular solutions of the 3D axisymmetric Euler equations. *Proc. Nat. Acad. Sci.* **111**, 12968–12973.
- Lundgren, T.S. 1982 Strained spiral vortex model for turbulent fine structure.. *Phys. Fluids* **25**, 2193.
- Meng, , & Yang, Y. 2024 Lagrangian dynamics and regularity of the spin Euler equation. *J. Fluid Mech* **985**, A34.
- Necas, J., Ruzicka, M., & Sverák, V. 1996 On Leray’s self-similar solutions of the Navier-Stokes equations. *Acta Math.* **176**, 283–294.
- Onsager, L. 1949 Statistical Hydrodynamics. *Il Nuovo Cimento, Suppl.* **6**, 279.
- Ostillo-Monico, R., McKeown, R., Brenner, M.P., Rubinstein, S.M., & Pumir, A. 2021 Cascades and reconnection in interacting vortex filaments. *Phys. Rev Fluids* **6**, 074701.

- Robinson, J.C., Rodrigo, J.L., & Sadowski, W. The Three-Dimensional Navier-Stokes Equations. Cambridge University Press, 2016.
- Robinson, J.C. 2020 . *Phil. Trans. R. Soc. A* **378**, 768320190526. The Navier–Stokes regularity problem.
- Robinson, J.C. 2021 Using periodic boundary condition to approximate the Navier-Stokes equations in \mathbb{R}^3 and the transfer of regularity.. *Nonlinearity* **34**, 7683.
- Schmitt, F., Fuchs, A., Peinke, J., & Obligado, M. 2024 Refined universality of the turbulence cascade. *arXiv:2407.15953v1* , .
- Sreenivasan, K.R. 1984 On the scaling of the energy dissipation rate. *Phys. Fluids* **27**, 1048..
- Vassilicos, J.C. 2015 Dissipation in Turbulent Flows. *Ann. Rev. Fluid Mech.* **47**, 95–114.
- Yao, J., & Hussain, F. 2020 A physical model of turbulence cascade via vortex reconnection sequence and avalanche.. *J. Fluid Mech.* **883**, A51.
- Yao, J., & Hussain, F. 2022 Vortex Reconnection and Turbulence Cascade. *Ann. Rev. Fluid Mech.* **54**, 317–347.
- Yao, J., & Yang, Y.F.Hussain 2021 Dynamics of a trefoil knotted vortex.. *J. Fluid Mech.* **923**, A19.
- Zuccoli, E., Brambley, E., & Barkley, D. 2024 Trapped Free Surface Waves for a Lamb–Oseen Vortex Flow. *J. Fluid Mech.* **997**, A40.